

Global Biogeochemical Cycles

RESEARCH ARTICLE

10.1029/2020GB006895

Key Points:

- Concentrations/fluxes of dissolved carbon, nitrogen, phosphorus, and major/trace ions were predominantly controlled by annual flood pulse
- Mean Amazon River dissolved organic carbon flux was 25.5 teragrams per year
- Annual carbonate + silicate weathering CO₂ consumption yield was 3.55×10^5 moles carbon dioxide per square kilometer

Supporting Information:

Supporting Information may be found in the online version of this article.

Correspondence to:

T. W. Drake,
draketw@gmail.com

Citation:









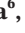



Drake, T. W., Hemingway, J. D., Kurek, M. R., Peucker-Ehrenbrink, B., Brown, K. A., Holmes, R. M., et al. (2021). The pulse of the Amazon: Fluxes of dissolved organic carbon, nutrients, and ions from the world's largest river. *Global Biogeochemical Cycles*, 35, e2020GB006895. <https://doi.org/10.1029/2020GB006895>

Received 20 NOV 2020

Accepted 28 FEB 2021

© 2021. American Geophysical Union.
All Rights Reserved.

The Pulse of the Amazon: Fluxes of Dissolved Organic Carbon, Nutrients, and Ions From the World's Largest River

Travis W. Drake¹ , Jordon D. Hemingway² , Martin R. Kurek³ , Bernhard Peucker-Ehrenbrink⁴ , Kristina A. Brown⁴ , Robert M. Holmes⁵ , Valier Galy⁴ , Jose M.S. Moura⁶ , Miyuki Mitsuya⁶ , Leonard I. Wassenaar⁷ , Johan Six¹ , and Robert G. M. Spencer³ 

¹Department of Environmental Systems Science, Swiss Federal Institute of Technology, ETH Zurich, Zurich, Switzerland, ²Department of Earth and Planetary Sciences, Harvard University, Cambridge, MA, USA, ³Department of Earth, Ocean, and Atmospheric Science, Florida State University, Tallahassee, FL, USA, ⁴Department of Marine Chemistry and Geochemistry, Woods Hole Oceanographic Institution, Woods Hole, MA, USA, ⁵Woodwell Climate Research Center, Falmouth, MA, USA, ⁶Universidade Federal do Oeste do Pará, Santarém-Tapajós, Brasil, ⁷Isotope Hydrology Section, International Atomic Energy Agency, Vienna, Austria

Abstract The Amazon River drains a diverse tropical landscape greater than 6 million km², culminating in the world's largest export of freshwater and dissolved constituents to the ocean. Here, we present dissolved organic carbon (DOC), organic and inorganic nitrogen (DON, DIN), orthophosphate (PO₄³⁻), and major and trace ion concentrations and fluxes from the Amazon River using 26 samples collected over three annual hydrographs. Concentrations and fluxes were predominantly controlled by the annual wet season flood pulse. Average DOC, DON, DIN, and PO₄³⁻ fluxes (± 1 s.d.) were 25.5 (± 1.0), 1.14 (± 0.05), 0.82 (± 0.03), and 0.063 (± 0.003) Tg yr⁻¹, respectively. Chromophoric dissolved organic matter absorption (at 350 nm) was strongly correlated with DOC concentrations, resulting in a flux of 74.8×10^6 m⁻² yr⁻¹. DOC and DON concentrations positively correlated with discharge while nitrate + nitrite concentrations negatively correlated, suggesting mobilization and dilution responses, respectively. Ammonium, PO₄³⁻, and silica concentrations displayed chemostatic responses to discharge. Major and trace ion concentrations displayed clockwise hysteresis (except for chloride, sodium, and rubidium) and exhibited either dilution or chemostatic responses. The sources of weathered cations also displayed seasonality, with the highest proportion of carbonate- and silicate-derived cations occurring during peak and baseflow, respectively. Finally, our seasonally resolved weathering model resulted in an average CO₂ consumption yield of $(3.55 \pm 0.11) \times 10^5$ mol CO₂ km⁻² yr⁻¹. These results represent an updated and temporally refined quantification of dissolved fluxes that highlight the strong seasonality of export from the world's largest river and set a robust baseline against which to gauge future change.

1. Introduction

On a global scale, rivers are important processors and conduits of terrestrially derived materials, transporting significant quantities of dissolved and particulate elements to downstream aquatic ecosystems, the atmosphere, and the ocean (Aufdenkampe et al., 2011; Gaillardet et al., 1999; Meybeck, 1982). In particular, the riverine fluxes of carbon (C), nitrogen (N), and phosphorus (P) represent important components of terrestrial net ecosystem production (NEP) and the transfer of energy and nutrients to lotic and marine ecosystems. Major and trace elements in rivers, on the other hand, reflect watershed geology, chemical weathering rates, and hydrology. The concentration, proportions, and fluxes of these elements in rivers represent integrated signals of the various processes that occur throughout the drainage basin, including mobilization, dilution, transport, transient storage, and weathering (Wohl, 2020). Time series datasets of concentration and water discharge allow for further refinement of annual flux estimates and can indicate the degree to which a given constituent is mobilized, diluted, or responds chemostatically with respect to discharge (Godsey et al., 2009; House & Warwick, 1998). Moreover, the geochemistry of rivers can be used to estimate the rate of continental denudation and the related consumption of atmospheric CO₂, one of the major goals of river geochemistry (Gaillardet et al., 1999).

As the largest river by discharge on Earth, the Amazon drains more than 6 million km² of dense tropical forests, floodplain forests (*Várzea*), snow-capped mountains, and savannas, culminating in a massive and diverse flux of dissolved constituents to the western equatorial Atlantic Ocean. Since the 1980s, a number of studies have quantified the concentration and fluxes of various dissolved constituents in the Amazon River, however many have relied on only a few measurements that were unevenly distributed across the seasonal hydrograph (Gaillardet et al., 1997; Moreira-Turcq et al., 2003; Richey et al., 1990). Given the Amazon Basin's distinct wet season, the mainstem experiences a pulse of water each year during which discharge can increase by a factor of two to three (Richey, Nobre, et al., 1989). Such seasonal variation in discharge has a profound effect on solute concentration and fluxes, which complicates extrapolations and exacerbates uncertainties of estimates made from smaller sporadic datasets. Furthermore, recent modeling has shown that proportion of terrestrial net primary productivity lost to the Amazon river displays significant interannual variation and dampens the interannual variability of NEP of the basin (Hastie et al., 2019), highlighting the need for longer time series data to detect these trends.

In addition to its natural variability, the Amazon River Basin is experiencing unprecedented change from anthropogenic activities. Ongoing climate change, in the form of increasing intensity of extreme weather events, increased flooding, longer drought periods, and prolonged fire seasons (Nobre et al., 2016), all have the capacity to alter the flux and composition of water and dissolved materials within the river. Deforestation from industrial logging and agricultural conversion also affects downstream riverine ecosystems via declines in rainfall, increases in runoff, soil disturbance, and erosion (Coe et al., 2009; Farella et al., 2001; Spencer et al., 2019; Spracklen & Garcia-Carreras, 2015). Deforestation also interacts with climate to exacerbate droughts, floods, and fire (Davidson et al., 2012; Nobre et al., 2016). On top of these climate and landscape-level changes, the rapid increase in the number of hydroelectric dams throughout the basin has resulted in further changes in hydrology and sediment transport (Anderson et al., 2018).

The detection of such projected change requires robust knowledge of present-day conditions. Here we present a contemporary dataset that includes the concentration and fluxes of dissolved organic carbon, organic and inorganic nitrogen, orthophosphate, and major and trace ions derived from 26 samples taken regularly over three annual hydrographs from 2011 to 2013 at Óbidos, Brazil, the furthest downstream gauging station on the Amazon River. Furthermore, using an ion source partitioning model, we provide a new, seasonally resolved estimate of CO₂ consumption via silicate and carbonate weathering in the basin. Given both the Amazon's predominant role in the global transport of dissolved materials to the ocean and the increasing severity of anthropogenic impacts on the basin, it is critical to refine seasonal concentration and flux estimates, evaluate interannual variability, and establish robust baselines in order to adequately assess the impact of future change.

2. Materials and Methods

2.1. Study Site

The hydrologic regime of the Amazon is governed by seasonal shifts in the Intertropical Convergence Zone (ITCZ), which create wet and dry seasons that alternate between north and south sides of the basin (Richey & Victoria, 1993). Annual precipitation varies considerably across the basin, but averages approximately 2,000 mm yr⁻¹ (Moreira-Turcq et al., 2003). The sheer size of the basin, low-interannual variability of average precipitation, lagged buffering of water from large tributaries, and the storage and passage of 30% of all the water in the river through the seasonal floodplain forests results in an interannually stable, monolithic pulse of water at the mainstem each year (Moreira-Turcq et al., 2003; Richey, Mertes, et al., 1989). Peak flows occur between May and August while low flows occur between September and December (Moreira-Turcq et al., 2003). Mainstem water discharge of the Amazon is commonly reported from Óbidos, the furthest downstream gauging station. It is important to note that Óbidos is still upstream of the “clearwater” tributaries, the Tapajos and Xingu. These tributaries contribute an additional ~17,000 m³ s⁻¹ of water (Ward et al., 2015) and ~50 kg C s⁻¹ to the river (Moreira-Turcq et al., 2003), which represent only ~9% and ~4% of the total water and OC fluxes for the Amazon system, respectively. At Óbidos, discharge ranges from ~89,000 to 260,000 m³ s⁻¹, a twofold to threefold difference between minimum (Q_{\min}) and maximum (Q_{\max}) discharge (Figure S1). Average discharge at Óbidos is ~180,000 m³ s⁻¹ (Figure S1). The primary interannual variability occurs on a two to three year timescale and is driven by the El Niño-Southern Oscillation (ENSO)



Figure 1. Amazon River Basin (highlighted area) with Óbidos sampling site (red point) and upstream drainage area (yellow outline).

cycle (Richey, Nobre, et al., 1989). This coupling between Amazon discharge and ENSO can be detected in discharge anomalies that vary inversely with Oceanic Niño Index, with a lag of approximately 6 months (Figure S2).

2.2. Sample Collection and Processing

Water samples were collected by boat approximately every month from July 2011 until November 2013 ($n = 26$) from the mainstem of the river at Óbidos (latitude 01.92409°S , longitude 55.52226°W ; Figure 1). To account for cross-channel heterogeneity, each sample consisted of a composite of three samples taken from 0.5 m depth at equally spaced intervals spanning the channel. Two liters collected from the center station were combined with one liter from each of the lateral stations into a 4 L carboy which was stored on ice in the dark until processing. A pole-mounted 1 L HDPE sample bottle, rinsed three times with river water, was used to collect water.

On the boat, unfiltered samples for water isotopes were taken with a peristaltic pump from the 4 L carboy composite after the sampling tube was rinsed with 500 mL of sample water. A 500 mL rinsed, in-line $0.45\ \mu\text{m}$ capsule filter (Geotech dispos-a-filter) was then used to fill two 1 L, acid-leached, polycarbonate bottles for dissolved organic matter (DOM) and nutrients and two 125 mL, acid-leached, HDPE bottles for major and trace elements. Each bottle was rinsed three times with filtered sample water prior to filling. To preserve the samples prior to transport and analyses, samples for DOM/nutrients and major/trace elements were frozen and refrigerated, respectively.

In situ water temperature, dissolved oxygen, conductivity, and pH were measured from the center of the river at a 0.5 m depth using a calibrated YSI Professional Plus multimeter.

2.3. Discharge, Precipitation, and Water Isotope Analyses

Amazon River discharge measurements (Q , $\text{m}^3 \text{s}^{-1}$) for the years 2009–2016 were derived from daily stage height measurements at Óbidos using an established discharge-stage rating curve maintained by Agência Nacional de Águas (<https://www.ana.gov.br/>; Figure S1). Monthly precipitation for years 2009–2016 at 0.1° resolution was derived from the NASA Global Precipitation Monitoring (GPM) v.6.0 data archive (Huffman et al., 2019), and catchment-averaged values were calculated as the mean of all pixels falling within the Amazon Basin area upstream of Óbidos.

Stable isotope (δD and $\delta^{18}\text{O}$) analyses of Amazon river water samples were conducted on field filtered samples and analyzed at the Isotope Hydrology Laboratory at the International Atomic Energy Agency, Vienna, Austria. Stable isotope analyses were conducted using a Picarro 2140i liquid water isotope analyzer system. We used eight water injections per sample vial and ignored the first four with data processing to correct for between-sample memory and normalization to the VSMOW2-SLAP2 scale by using LIMS for Lasers 2015 (Coplen & Wassenaar, 2015). The δD and $\delta^{18}\text{O}$ values relative to VSMOW for the laboratory standards were $+25.4 \pm 0.8$ and $+3.63 \pm 0.04$ ‰ for W-39, and -189.5 ± 0.9 , -24.78 ± 0.02 ‰ for W-34. The analytical uncertainty for δD and $\delta^{18}\text{O}$ for the river water samples was better than ± 0.7 and ± 0.1 ‰, respectively.

2.4. Dissolved Carbon, Nitrogen, Phosphate, Silica, and UV-Absorbance Analyses

Dissolved organic carbon (DOC) and total dissolved nitrogen (TDN) concentrations were determined via high-temperature combustion on a Shimadzu TOC-V total organic carbon analyzer paired with a nitrogen chemiluminescence detection unit (TNM-1) using established methodology (Mann et al., 2012). DOC and TDN concentrations were calculated as the mean of at least three injections for which the coefficient of variation was less than 2%. Inorganic nutrients (nitrate + nitrite, $\text{NO}_3^- + \text{NO}_2^-$; ammonium, NH_4^+ ; orthophosphate, PO_4^{3-} ; and silica, SiO_2) were analyzed on an Astoria Analyzer using acidified aliquots of filtered sample water following established methods (Mann et al., 2012). Dissolved organic nitrogen (DON) was calculated by subtracting dissolved inorganic nitrogen ($\text{DIN} = \text{NO}_3^- + \text{NO}_2^- + \text{NH}_4^+$) from TDN.

UV-visible absorbance from 200 to 800 nm was measured on a Shimadzu dual beam UV-1800 spectrophotometer using established methodology (Mann et al., 2012). Samples were analyzed at room temperature and blank corrected with DI water. Absorbance data presented in this study are expressed as absorption coefficients, $a(\lambda)$, in units of m^{-1} (Hu et al., 2002). Napierian chromophoric DOM (CDOM) absorption coefficients were calculated as

$$a(\lambda) = 2.303A(\lambda) / l \quad (1)$$

where $A(\lambda)$ is the measured absorbance (in nm) and l is the length of the cell path in meters (0.01 m for this study).

2.5. Dissolved Ion Analyses

Anion concentrations (Cl^- , SO_4^{2-}) were determined using a Dionex ion chromatography (IC) system following Voss et al. (2014) with a few minor modifications. Briefly, undiluted sample water was injected twice on an anion column (IonPacAS15, 4 mm, with ASRS 300 suppressor) and eluted with 50% 75 mM NaOD and 50% Milli-Q H_2O . Analytical response was evaluated against serial dilutions of an internal standard (SpecPure ion chromatography standards; Alfa Aesar) as well as International Association for the Physical Sciences of the Oceans standard seawater certified reference material (CRM, Batch P160). Concentrations were calculated based on 5-point standard calibration curves using Chromeleon software, with no blank correction applied. CRM concentrations were always within $\pm 3\%$ of reported values for anions measured.

Major cation (Na^+ , Mg^{2+} , K^+ , Ca^{2+}) and trace element (Li^+ , Sr^{2+} , Rb^+ , Ba^{2+} , U) concentrations were analyzed by single collector, inductively coupled plasma, magnetic sector mass spectrometry (ICP-MS) using the Thermo Scientific Element2 ICP-MS of the WHOI Plasma Facility, following methods described in Voss et al. (2014) and Brown et al. (2020). In a clean laboratory, about 1.8 mL river water was pipetted into 2 mL screw-cap autosampler vials and centrifuged for 10 min at 7000 rpm. About 1 mL of the supernatant was

pipetted into another 2 mL autosampler vial to which small amounts of indium and rhenium internal standards and sufficient concentrated HNO_3 were added to adjust the pH of the solution to ≤ 2 . The concentrations of the internal standard isotopes were adjusted such that typical count rates were $\sim 500,000$ counts per second (cps, $10^{11} \Omega$ resistor). The ICP-MS detector response was tuned on scandium, indium, and uranium isotopes for maximum stable ion beam intensities. Sample vials were put on a vibrating shaker before being loaded into an autosampler and analyzed by self-aspiration at low ($m/\Delta m \sim 300$ for Rb^+ , Sr^{2+} , Ba^{2+}), medium ($m/\Delta m \sim 3000$, Ca^{2+}) and high ($m/\Delta m \sim 10,000$, Na^+ , Mg^{2+} , K^+) mass resolving powers. Calibration of concentrations was done with seven-point standard calibration curves using serial dilutions of NIST 1640a and SLRC-5 (National Research Council Canada) as certified reference materials. Whenever possible, count rates were collected for more than one isotope per element in order to check for the presence of isobaric interferences. Analytical blanks were prepared identical to river water samples with the exception that Milli-Q water (Millipore, $18.2 \text{ M}\Omega \text{ cm}$) replaced river water. Analytical results are corrected for blank, drift and isobaric interferences. External reproducibility (2 s.d.) is generally better than $\pm 5\%$.

2.6. Data Analyses

Concentrations that either exceeded the third quartile + $1.5\times$ the interquartile range (IQR) or were less than the first quartile - $1.5\times$ the IQR ($n = 14$) were determined to be statistical outliers and removed from the flux analyses (Tukey, 1977). Linear and power law equations were fit to the data using least squares regressions with the Prism Graphpad statistical software. For all regressions, 95% confidence intervals were also calculated. Physical parameters (temperature, dissolved oxygen, water isotopes) relationships with discharge were fitted with linear regressions. Conductivity and concentration-discharge data were fit with the power law equation:

$$C = a * Q^b \quad (2)$$

where C is the solute concentration or conductivity, Q is the water discharge, and a and b are fitted constants. The value of the exponent (b) indicates the influence of mobilization (positive values), dilution (negative values) or chemostasis (close to zero) (Bouchez et al., 2017; Godsey et al., 2009). The power law equation has become the preferred model for concentration-discharge relationships given the utility of the b -exponent as a quantitative metric to evaluate C-Q patterns (Musolf et al., 2015; Rose et al., 2018).

2.7. Flux Estimates

Daily fluxes (kg d^{-1}) for all carbon, nutrient, and major and trace ions were modeled using instantaneous discharge measurements (2011–2013) and concentration data input into the FORTRAN Load Estimator (LOADEST) program (Runkel et al., 2004). Daily fluxes ($\text{m}^2 \text{ d}^{-1}$) for CDOM at absorbance 350 nm (a_{350}) were also modeled using LOADEST. Units for CDOM flux ($\text{m}^2 \text{ d}^{-1}$) result from the product of absorbance (m^{-1}) and daily discharge ($\text{m}^3 \text{ d}^{-1}$). Daily fluxes for each year were then summed to generate annual fluxes. For each constituent, the LOADEST calibration equation was determined using the Adjusted Maximum Likelihood Estimator (AMLE) with the regression model number set to default (MODNO = 0), allowing the model to select the best fit using Akaike Information Criteria. The model output provides the standard error and the standard error of the prediction of the fluxes along with the r^2 of the AMLE, residuals, and the serial correlation of the residuals. These outputs allow for validation of the model and for confirmation that the residuals are normally distributed according to established protocols (Dornblaser & Striegl, 2009).

2.8. Weathering Model

Silicate- and carbonate-rock weathering CO_2 consumption fluxes were estimated using a modified version of the ion source partitioning model described in Torres et al. (2016). Dissolved riverine Ca^{2+} , Cl^- , K^+ , Mg^{2+} , Na^+ , Sr^{2+} , and SO_4^{2-} ions were assumed to be sourced from a mixture of dolomite (D), evaporitic gypsum and halite (E), cratonic silicate rocks (G), limestone (L), precipitation (P), or shale rock (S) end members. The charge abundances of each ion X ($= \text{Ca}^{2+}$, Cl^- , K^+ , Mg^{2+} , Na^+ , Sr^{2+} , or SO_4^{2-}) normalized to total base cation charge equivalents were used as conservative tracers. Normalized abundances were calculated as

$$\chi_X^i = \frac{|Z_X|[X]^i}{\Sigma^{+,i}} \quad (3)$$

where $|Z_X|$ is the absolute value of the valence of ion X , $[X]$ is the concentration of ion X , Σ^+ is the base cation charge equivalents defined as

$$\Sigma^+ = 2[Ca^{2+}] + [K^+] + 2[Mg^{2+}] + [Na^+] \quad (4)$$

and $i = D, E, G, L, P$, or S refers to a specific end member whereas $i = R$ refers to measured riverine values. Because the number of conservative tracers is greater than the number of end members, fractional contributions of each end member to measured riverine ion loads were determined using a least-squares regression subject to the constraint that solutions must be non-negative. That is, we solved

$$\min_{X \geq 0} \|AX - B\| \quad (5)$$

where \mathbf{A} is the $[n_{\text{tracer}}+1 \times n_{\text{end member}}]$ design matrix of end member χ_X^i values, \mathbf{B} is the $[n_{\text{tracer}}+1 \times n_{\text{sample}}]$ matrix of measured χ_X^R values, and \mathbf{X} is the $[n_{\text{end member}} \times n_{\text{sample}}]$ matrix of resulting end-member fractional contribution estimates. The final row of both \mathbf{A} and \mathbf{B} is set to unity to satisfy the sum-to-unity constraint.

End member χ_X^i values are not perfectly known *a priori* and often exhibit considerable uncertainty. To account for such uncertainty, a Monte Carlo approach was utilized. For each of 10,000 iterations, (i) the \mathbf{A} matrix was recalculated by randomly sampling each χ_X^i value from within its *a priori* range (i.e., a bounded uniform distribution), (ii) Equation 5 was solved, and (iii) the model-data misfit root mean square error (RMSE) was calculated as

$$RMSE = \left(\frac{\|AX - B\|^2}{n_{\text{sample}}} \right)^{1/2} \quad (6)$$

Following Torres et al. (2016), the 100 iterations exhibiting the lowest RMSE values (i.e., 1% of total iterations) were retained as acceptable solutions. By only retaining the \mathbf{A} matrices corresponding to the lowest RMSE, this approach additionally provides a *posteriori* constraints on end-member χ_X^i values.

For this study, dolomite, evaporite, limestone, and shale χ_X^i ranges were taken as bulk-rock values reported in Torres et al. (2016), whereas cratonic silicate rock χ_X^i ranges were calculated using sodium-normalized concentrations for monolithological tributaries draining the Guayana and Brazilian shields (Gaillardet et al., 1997), as these represent the dominant silicate end-member within the drainage basin. Precipitation ionic compositions were taken to be equal to that of seawater; our model therefore treats the observed Ca^{2+} , Mg^{2+} , K^+ , and Sr^{2+} surpluses in Amazon basin rainwater relative to seawater as originating from rock weathering within the basin (so-called “cyclic” inputs), as is common practice (e.g., Gaillardet et al., 1997). All *a priori* and *a posteriori* end-member χ_X^i ranges are reported in Table S1.

Finally, total silicate ($G + S$) and carbonate ($D + L$) weathering-derived base cation charge concentrations were determined by multiplying resulting fractional end-member contributions by measured $\Sigma^{+,R}$ at each time point; concentrations were converted to annual averaged charge yields using LOADEST as described in Section 2.7 and dividing by total basin area upstream of Óbidos. CO_2 consumption yields ($\text{mol } CO_2 \text{ km}^{-2} \text{ yr}^{-1}$) were taken as equal to charge yield for silicate rock weathering and equal to 50% of charge yield for carbonate rock weathering since half of resulting carbonate alkalinity is sourced from rock-derived CO_3^{2-} (e.g., Probst et al., 1994). This approach assumes that all weathering proceeds *via* carbonic acid and implicitly ignores weathering by sulfuric acid (cf., Torres et al., 2016); CO_2 consumption yields reported here should thus be treated as maximum values.

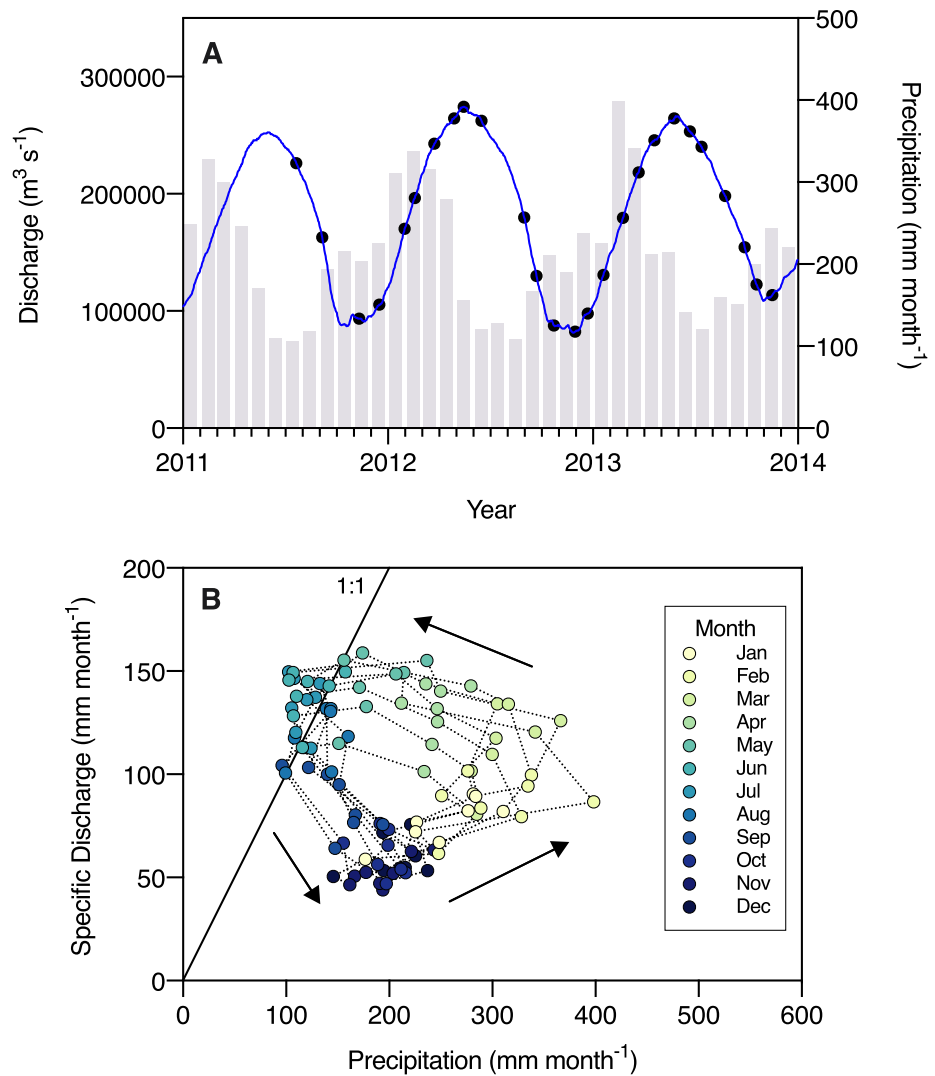


Figure 2. (a) Instantaneous discharge (blue line) for 2011–2013 with sampling dates (black dots) and monthly precipitation (gray bars). (b) Monthly specific discharge (discharge/drainage area) versus monthly precipitation for 2009–2016, colored by month of the year.

3. Results

3.1. Hydrologic Setting, In Situ Parameters, and Water Isotopes

Amazon River discharge measured daily at the Óbidos gauging station for the three-year study period ranged from $81,431$ to $274,383 \text{ m}^3 \text{ s}^{-1}$ (Figure 2a). The range of instantaneous discharge at the time of the sampling events spanned 99.5% of this range ($82,451$ – $274,383 \text{ m}^3 \text{ s}^{-1}$, Table 1). Peak discharge was consistent (mean = $264,307 \text{ m}^3 \text{ s}^{-1}$, coefficient of variation [c.v.] = 4.2%) while the minimum showed more variability (mean = $91,150 \text{ m}^3 \text{ s}^{-1}$; c.v. = 13.5%). The typical, steady, and singular wet-season flood pulse of water that culminates in the seasonal maximum in June was evident in all three study years (Figure 2a). The average intra-annual variability (daily $\text{max}Q/\text{min}Q$) was 2.93, with the highest value in 2012 (3.37) when discharge exhibited both the lowest minimum and highest maximum. Total annual discharge was lowest in 2011 ($5,355 \text{ km}^3 \text{ yr}^{-1}$) and higher in 2012 and 2013 ($5,845$ and $5,920 \text{ km}^3 \text{ yr}^{-1}$, respectively; Table 2).

Discharge at Óbidos displayed prominent, annual counterclockwise hysteresis relative to precipitation for years 2009–2016 (Figure 2b). Average monthly precipitation peaked in January to February (250 – $400 \text{ mm month}^{-1}$) whereas specific discharge (discharge/upstream basin area) at Óbidos generally peaked four

Table 1

Instantaneous Discharge, Water Temperature, Dissolved Oxygen, Conductivity, pH, and Water Isotopes for all 26 Samplings at Óbidos

Sample ID (IGSN)	Date	Q (m ³ s ⁻¹)	Water Temp. (°C)	D.O. (%)		Cond. (μS cm ⁻¹)	pH	δD-H ₂ O (‰)	δ ¹⁸ O-H ₂ O (‰)
GRO001347	Jul 22, 2011	226,330	-	-	-	-	-	-43.1	-6.9
GRO001348	Sep 06, 2011	162,872	-	-	-	-	-	-31.5	-5.6
GRO001349	Nov 11, 2011	93,346	30.5	77.7	5.82	66.3	7.2	-22.0	-4.6
GRO001350	Dec 17, 2011	105,462	30.4	73.1	5.49	66.4	7.1	-32.7	-5.8
GRO001351	Jan 31, 2012	170,061	29.3	57.5	4.50	66.1	7.3	-37.9	-6.4
GRO001352	Feb 18, 2012	196,409	28.0	55.6	4.33	60.2	7.0	-35.5	-6.2
GRO001353	Mar 24, 2012	242,676	28.0	42.6	3.32	50.5	7.0	-39.1	-6.5
GRO001354	Apr 28, 2012	264,423	28.7	31.6	2.45	43.2	6.9	-39.8	-6.6
GRO001355	May 15, 2012	274,383	28.6	32.1	2.46	43.0	7.2	-42.2	-6.7
GRO001356	Jun 16, 2012	262,324	27.8	38.6	3.03	55.7	6.8	-44.5	-7.3
GRO001357	Aug 16, 2012	179,839	29.7	51.1	3.86	41.0	7.3	-25.5	-5.0
GRO001358	Sep 22, 2012	129,870	30.6	65.0	4.79	45.2	6.8	-20.8	-4.4
GRO001359	Oct 23, 2012	87,695	30.8	80.9	5.96	62.1	7.3	-19.0	-4.0
GRO001360	Nov 30, 2012	82,451	31.1	77.5	5.59	67.7	7.2	-23.5	-4.6
GRO001361	Dec 22, 2012	97,760	29.7	84.2	6.39	72.0	7.6	-26.9	-5.0
GRO001362	Jan 19, 2013	130,902	29.2	70.8	5.42	72.6	7.7	-33.4	-5.9
GRO001363	Feb 23, 2013	179,576	28.4	66.1	5.11	64.3	7.3	-30.5	-5.4
GRO001364	Mar 23, 2013	218,322	28.4	55.5	4.27	49.5	6.5	-33.5	-5.8
GRO001365	Apr 20, 2013	245,650	29.0	39.1	2.99	48.8	6.4	-35.6	-6.0
GRO001366	May 25, 2013	264,423	28.9	41.0	3.23	44.9	7.0	-37.3	-6.1
GRO001367	Jun 22, 2013	253,375	29.0	83.9	6.43	45.1	8.3	-41.3	-6.8
GRO001368	Jul 13, 2013	240,055	28.8	63.0	4.93	45.0	7.9	-38.3	-6.7
GRO001369	Aug 24, 2013	198,099	28.8	91.7	7.02	41.4	7.8	-28.8	-5.5
GRO001370	Sep 28, 2013	154,501	30.2	-	-	42.7	6.1	-22.6	-4.7
GRO001371	Oct 19, 2013	122,617	30.9	-	-	47.5	6.8	-19.3	-4.2
GRO001372	Nov 16, 2013	113,611	-	-	-	-	-	-20.3	-4.6
Min	-	82,451	27.8	31.6	2.45	41.0	6.1	-44.5	-7.3
Max	-	274383	31.1	91.7	7.02	72.6	8.3	-19.0	-4.0
Average	-	180,655	29.4	60.9	4.64	54.0	7.1	-31.7	-5.7
s.d.	-	64,156	1.0	18.5	1.36	11.0	0.5	8.1	0.9
c.v. (%)	-	35.5	3.4	30.4	29.3	20.3	6.9	25.6	16.7

Note: Dashes indicate missing data. Minimum (blue), maximum (red), average (bold), standard-deviation (s.d.), and coefficient of variation (c.v.) are also presented. Coefficients of variation are highlighted in a grayscale gradient from lowest (white) to highest (gray).

months later (130–155 mm month⁻¹, Figure 2b). Monthly precipitation exceeded specific discharge (below the 1:1 line, Figure 2b) throughout the year except for peak flows in May–June, when it was approximately equal (Figure 2b). Averaged annually throughout the basin, precipitation was 2.02 ± 0.18 times greater than specific discharge at Óbidos (*n* = 8 years).

Amazon River water temperature at Óbidos was stable throughout the study period (c.v. = 3.4%), ranging from 27.8 to 31.1 °C (Table 1). Despite the narrow range, water temperature was negatively correlated with discharge when modeled with a linear function (*r*² = 0.67, *p* < 0.0001), decreasing by ~2.5 °C from minimum to peak discharge (Figure 3a). Water temperature exhibited slight hysteresis relative to discharge,

Table 2
Annual Water, Dissolved Organic Carbon, Chromophoric Dissolved Organic Matter (CDOM at 350 nm), Silica, Dissolved Organic Nitrogen, Nitrate + Nitrite, Ammonium, and Orthophosphate Fluxes, Areal Yields (Upstream of Óbidos), and Discharge-Weighted Average Concentrations From the Amazon River for Years 2011, 2012, and 2013

Q (km ³ yr ⁻¹)	DOC			a ₃₅₀			SiO ₂			DON			NO ₃ ⁻ + NO ₂ ⁻			NH ₄ ⁺			PO ₄ ³⁻		
	Flux (Tg yr ⁻¹)	Yield (g m ⁻² yr ⁻¹)	Q-W.A.C. (mg L ⁻¹)	Flux (10 ¹² m ³ yr ⁻¹)	Yield (m ⁻¹)	Q-W.A.A. (m ⁻¹)	Flux (Tg yr ⁻¹)	Yield (g m ⁻² yr ⁻¹)	Q-W.A.C. (mg L ⁻¹)	Flux (Gg yr ⁻¹)	Yield (g m ⁻² yr ⁻¹)	Q-W.A.C. (µg L ⁻¹)	Flux (Gg yr ⁻¹)	Yield (mg m ⁻² yr ⁻¹)	Q-W.A.C. (µg L ⁻¹)	Flux (Gg yr ⁻¹)	Yield (mg m ⁻² yr ⁻¹)	Q-W.A.C. (µg L ⁻¹)	Flux (Gg yr ⁻¹)	Yield (mg m ⁻² yr ⁻¹)	Q-W.A.C. (µg L ⁻¹)
2011	5355	24.6	4.60	74.7	16.0	13.95	42.2	9.03	7.88	1.14	0.24	0.21	797	0.17	149	36.3	7.76	6.8	60.3	12.9	11.3
2012	5845	26.6	4.55	78.0	16.7	13.35	48.9	10.45	8.36	1.19	0.25	0.20	756	0.16	129	45.9	9.82	7.9	64.7	13.8	11.1
2013	5920	25.3	4.42	71.8	15.3	12.12	53.0	11.34	8.96	1.09	0.23	0.18	775	0.17	131	53.1	11.36	9.0	65.6	14.0	11.1
Average	5707	25.5	4.47	74.8	16.0	13.14	48.0	10.27	8.40	1.14	0.24	0.20	776	0.17	136	45.1	9.64	7.9	63.5	13.6	11.1
s.d.	307	1.0	0.21	3.1	0.7	0.93	5.5	1.17	0.54	0.05	0.01	0.02	20	0.004	11	8.5	1.81	1.1	2.8	0.6	0.1
c.v. (%)	5.4	3.9	3.89	4.2	4.2	7.1	11.4	11.4	6.4	4.4	4.4	7.6	2.6	2.6	7.9	18.7	18.7	14.0	4.4	4.4	4.4

Note: All mass units refer to the single atom (C, N, or P) rather than the molecule, except for silica. Three-year averages are presented in bold with standard-deviation (s.d.) and coefficient of variation (c.v.) below. Coefficients of variation are highlighted in a grayscale gradient from lowest (white) to highest (gray).

with rising limb temperatures (red points) ~1° colder than those at equivalent discharge during the falling limb (blue points, Figure 3a). Dissolved oxygen (DO) concentrations ranged from 2.45 to 7.02 mg L⁻¹ (equivalent to 31.6%–91.7% saturation), with a mean of 4.64 mg L⁻¹ (Table 1). DO concentration was also negatively correlated with discharge when modeled with a linear function ($r^2 = 0.46$, $p = 0.0008$), decreasing by ~3.5 mg L⁻¹ from minimum to peak discharge (Figure 3b). Conductivity ranged from 41.0 to 72.6 µS cm⁻¹, with a mean of 54 µS cm⁻¹ (Table 1). Conductivity, modeled with a power function, exhibited a moderate dilution response with rising discharge (b -value = -0.32, $r^2 = 0.43$) and clockwise hysteresis during the rising and falling limbs of the annual flood pulse (Figure 3c). pH ranged from 6.1 to 8.3 (Table 1) but did not vary significantly with discharge (Figure 3d).

Stable isotope values (δD and $\delta^{18}O$) of Amazon River water fell close to the Brazil local meteoric water line (Brazil LMWL; IAEA/WMO, 2020), with slightly elevated δD values at high $\delta^{18}O$ and a deuterium excess (d) value of 16.4‰ (Figure 4a). Hydrogen isotopic signatures of water ranged from -44.5 to -19.0‰ (Table 1), with a discharge-weighted annual mean of -35.8‰. Oxygen isotopic signatures of water ranged from -7.3 to -4.0‰ (Table 1), with a discharge-weighted annual mean of -6.1‰. Both δ^2D and $\delta^{18}O$ were negatively correlated with discharge ($r^2 = 0.68$ and 0.62 , p -values < 0.0001, respectively), such that the isotopes were enriched at minimum discharge and depleted at peak discharge (Figures 4b and 4c, respectively). δD and $\delta^{18}O$ also exhibited slight counterclockwise hysteresis, such that isotopic values on the rising limb of the hydrograph were more depleted in deuterium and ¹⁸O compared to the values during the equivalent discharge on the falling limb (Figures 4b and 4c, respectively).

3.2. Dissolved Organic Carbon, Nitrogen, and Orthophosphate

3.2.1. Concentrations

Amazon River DOC concentrations ranged from 2.86 to 5.23 mg C L⁻¹, with a mean of 4.19 mg C L⁻¹ (Table 3). DOC concentrations exhibited a strong positive correlation with discharge (b -value = 0.39, $r^2 = 0.77$) and slight clockwise hysteresis at flows greater than 150,000 m³ s⁻¹ (Figure 5a). DON concentrations ranged from 0.11 to 0.41 mg N L⁻¹, with a mean of 0.20 mg N L⁻¹ (Table 3). Like DOC, DON concentrations were positively correlated with discharge, albeit with a weaker relationship (b -value = 0.38, $r^2 = 0.43$; Figure 5b). Silica (SiO₂) concentrations spanned a range from 7.56 to 15.00 mg L⁻¹ (mean = 9.03 mg L⁻¹; Table 3) and did not vary significantly with discharge (b -value = -0.06, $r^2 = 0.04$; Figure 5c). Nitrate plus nitrite (NO₃⁻ + NO₂⁻) concentrations ranged from 81.2 to 286.8 µg N L⁻¹ (mean = 150.8 µg N L⁻¹; Table 3) and were strongly negatively correlated with discharge (b -value = -0.78, $r^2 = 0.69$; Figure 5d). NO₃⁻ + NO₂⁻ concentrations also exhibited clear clockwise hysteresis, with higher values during the rising limb of the seasonal flood pulse compared to equal magnitude flows during the falling limb (Figure 5d). Orthophosphate (PO₄³⁻) concentrations ranged from 5.97 to 15.98 µg P L⁻¹ (mean = 11.37 µg P L⁻¹; Table 3) and displayed an insignificant relationship with discharge (b -value = 0.20, $r^2 = 0.20$; Figure 5e). Ammonium (NH₄⁺) concentrations ranged from 5.91 to 14.56 µg N L⁻¹ (mean = 8.29 µg N L⁻¹; Table 3) and also displayed no relationship with discharge (b -value = -0.20, $r^2 = 0.14$; Figure 5f).

3.2.2. LOADEST Fluxes, Yields, and Discharge-Weighted Concentrations

The mean annual DOC flux from the Amazon River at Óbidos was 25.5 Tg C yr⁻¹ and was consistent across the three study years (s.d. = 1.0 Tg, c.v. = 3.9%; Table 2). The strong positive relationship between DOC concentration and discharge resulted in a compounding effect for the seasonal fluxes, which increased by an average factor of 4.6 from low to high flows and were highly synchronized with the seasonal flood pulse (Figure 6a). Mean annual DOC yield and discharge-weighted concentration was 5.45 g C m⁻² yr⁻¹ and

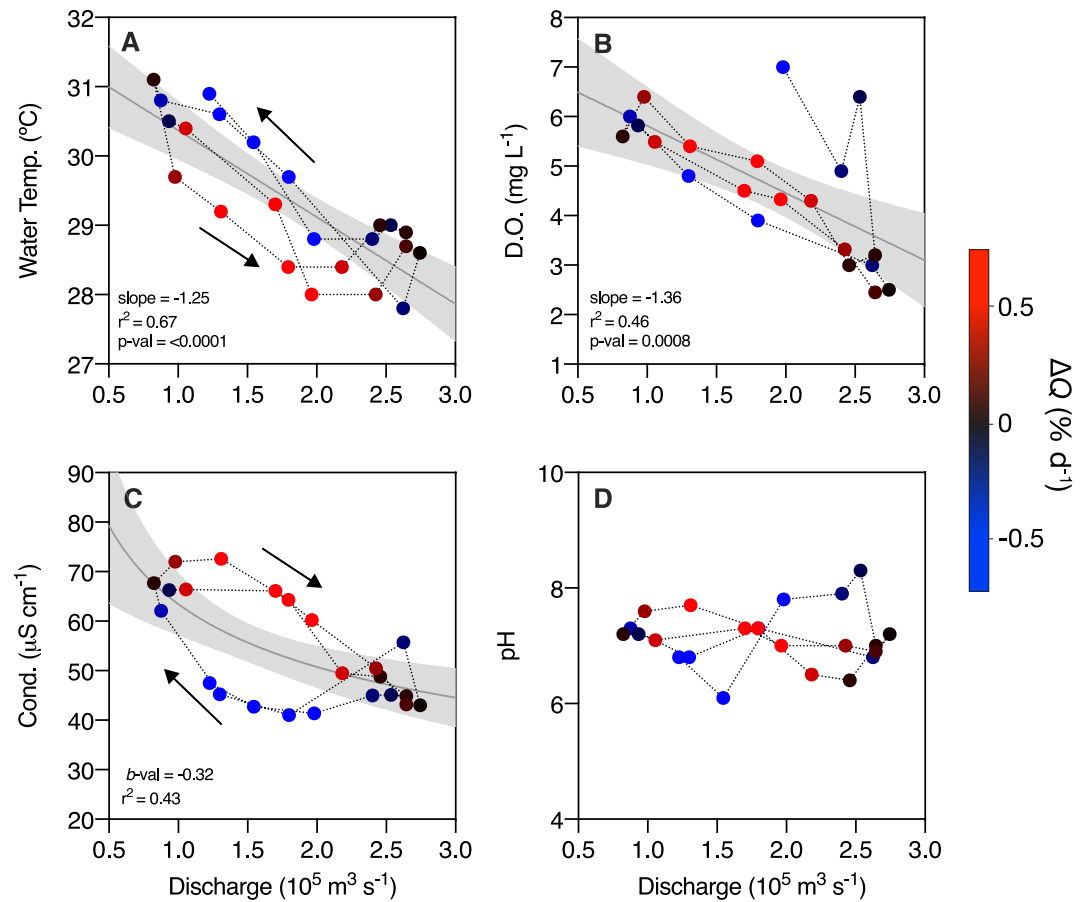


Figure 3. Water temperature (a), dissolved oxygen (b), conductivity (c), and pH (d) as a function of instantaneous discharge. Data points are colored by instantaneous change in discharge with red indicating an increasing flow (rising limb) and blue indicating decreasing flow (falling limb). Linear or power regressions (gray line) are shown with 95% confidence intervals (light gray bands) for water temperature, dissolved oxygen, and conductivity.

4.47 mg C L^{-1} , respectively (Table 2). Mean annual DON flux was 1.14 Tg N yr^{-1} (Table 2) and, like DOC flux, was highly synchronized with discharge (Figure 6b). Mean annual DON yield and discharge-weighted concentration were 0.24 $\text{g N m}^{-2} \text{ yr}^{-1}$ and 0.20 mg N L^{-1} , respectively (Table 2). Average annual SiO_2 flux was 48.0 Tg yr^{-1} with higher interannual variability (c.v. = 11.4%) as a result of a consistent rise in fluxes throughout the study period (+5.8 Tg ; Table 2, Figure 6c). Mean annual SiO_2 yield and discharge-weighted concentration were 10.27 $\text{g m}^{-2} \text{ yr}^{-1}$ and 8.40 mg L^{-1} , respectively (Table 2). Mean annual $\text{NO}_3^- + \text{NO}_2^-$ flux was 776 Gg N yr^{-1} (Table 2). Peak $\text{NO}_3^- + \text{NO}_2^-$ fluxes arrived during the rising limb of the seasonal flood pulse, approximately 105 days earlier than peak discharge (Figure 6d). A second, smaller flux peak occurred during the falling limb of each of the study years, indicating a moderate hysteresis effect (Figure 6d). Both of these limb peaks were a result of the inverse relationship between $\text{NO}_3^- + \text{NO}_2^-$ concentrations and discharge (Figure 5d), since the product of discharge and concentration (flux) was optimized between low and high flow regimes. Mean annual $\text{NO}_3^- + \text{NO}_2^-$ yield and discharge-weighted concentration were 0.17 $\text{g m}^{-2} \text{ yr}^{-1}$ and 136 $\mu\text{g N L}^{-1}$, respectively (Table 2). Annual PO_4^{3-} fluxes increased slightly over the study period (+5.3 Gg), but had a mean of 63.5 Gg yr^{-1} (Table 2). Peak PO_4^{3-} fluxes were synchronized with discharge (Figure 6e). Mean annual PO_4^{3-} yield and discharge-weighted concentration were 13.6 $\text{mg P m}^{-2} \text{ yr}^{-1}$ and 11.1 $\mu\text{g P L}^{-1}$ (Table 2). NH_4^+ fluxes were synchronized with the seasonal flood pulse (Figure 6f) but exhibited high interannual variation (c.v. = 18.7%) as a result of a sizable increase through the three-year study period (+16.8 Gg yr^{-1} ; Table 2). Mean NH_4^+ flux, annual yield, and discharge-weighted concentration were 45.1 Gg yr^{-1} , 9.64 $\text{mg m}^{-2} \text{ yr}^{-1}$, and 7.9 $\mu\text{g N L}^{-1}$, respectively (Table 2).

Table 3
Instantaneous Discharge, Dissolved Constituent Concentrations, and Chromophoric Dissolved Organic Matter for all 26 Amazon River Samples used in this Study

Date	Q (m ³ s ⁻¹)	DOC (mg C L ⁻¹)	a ₃₅₀ (m ⁻¹)	DON (mg N L ⁻¹)	NO ₃ ⁻ +NO ₂ ⁻ (μg N L ⁻¹)	NH ₄ ⁺ (μg N L ⁻¹)	PO ₄ ³⁻ (μg P L ⁻¹)	SiO ₂ (mg L ⁻¹)	Ca ²⁺ (μM)	Mg ²⁺ (μM)	Na ⁺ (μM)	Cl ⁻ (μM)	SO ₄ ²⁻ (μM)	K ⁺ (μM)	Li ⁺ (μM)	Rb ⁺ (nM)	Sr ²⁺ (nM)	Ba ²⁺ (nM)	U (nM)
Jul 22, 2011	226,330	4.92	14.47	0.19	106	6.2	6.0	7.79	135	37	79	38	19	23	93	18	340	163	0.24
Sep 06, 2011	162,872	3.87	11.94	0.24	138	7.3	8.9	8.20	122	34	83	40	20	19	85	18	310	145	0.18
Nov 11, 2011	93,346	3.52	10.76	0.20	208	5.9	12.3	8.24	176	50	132	65	44	25	115	21	441	164	0.23
Dec 17, 2011	105,462	4.14	11.68	0.19	234	7.0	11.7	8.15	178	49	125	65	48	25	115	21	451	175	0.33
Jan 31, 2012	170,061	4.40	12.84	0.41	207	6.7	13.1	8.17	217	59	93	42	44	27	119	18	531	193	0.35
Feb 18, 2012	196,409	4.72	13.85	0.19	163	7.9	11.7	8.05	206	55	80	33	37	26	116	18	505	193	0.36
Mar 24, 2012	242,676	4.93	14.90	0.37	115	6.4	8.8	8.18	175	49	69	29	31	26	113	18	427	180	0.30
Apr 28, 2012	264,423	5.09	15.40	0.21	86	9.3	9.1	7.56	138	41	60	23	22	24	108	20	347	171	0.29
May 15, 2012	274,383	4.65	14.84	0.20	83	14.6	10.6	7.81	140	41	63	25	21	24	102	20	351	175	0.24
Jun 16, 2012	262,324	5.23	13.76	0.22	83	6.4	9.1	8.12	161	45	77	35	22	25	97	21	401	195	0.23
Aug 31, 2012	179,839	3.77	12.42	0.16	124	7.5	11.8	15.00	124	34	78	37	19	21	84	20	309	155	0.20
Sep 22, 2012	129,870	3.71	10.89	0.15	145	10.4	10.8	9.97	131	37	96	47	23	22	84	22	329	156	0.21
Oct 23, 2012	87,695	2.86	9.67	0.11	192	7.1	14.9	9.59	186	49	143	74	37	24	94	23	454	182	0.22
Nov 30, 2012	82,451	3.40	9.57	0.13	238	8.7	15.1	12.25	198	56	151	76	49	26	118	22	494	185	0.22
Dec 22, 2012	97,760	3.21	8.54	0.11	243	7.7	16.0	8.61	214	61	149	75	56	28	121	20	532	189	0.23
Jan 19, 2013	130,902	3.61	9.18	0.15	287	6.1	12.1	8.32	237	67	114	47	59	30	129	18	577	207	0.25
Feb 23, 2013	179,576	4.67	12.66	0.34	174	9.1	10.2	9.35	217	61	93	38	42	30	129	19	528	209	0.35
Mar 23, 2013	218,322	5.02	14.47	0.25	130	8.9	15.6	9.49	161	46	70	29	30	26	116	19	400	179	0.31
Apr 20, 2013	245,650	4.88	13.62	0.22	93	9.6	9.8	8.42	159	46	66	28	26	27	119	21	399	187	0.26
May 25, 2013	264,423	5.09	13.82	0.23	81	10.4	10.8	10.91	149	41	67	28	19	24	96	21	374	182	0.23
Jun 22, 2013	253,375	4.61	13.09	0.17	83	10.5	14.4	8.96	145	41	74	36	20	22	95	20	365	180	0.24
Jul 13, 2013	240,055	4.28	12.53	0.19	89	9.8	10.9	8.42	140	37	73	35	20	21	86	20	349	173	0.22
Aug 24, 2013	198,099	3.77	10.93	0.23	114	10.1	9.8	7.92	129	34	79	39	21	20	90	19	319	155	0.22
Sep 28, 2013	154,501	3.90	11.33	0.16	127	9.0	9.8	7.94	127	34	87	46	23	19	88	20	316	154	0.25
Oct 19, 2013	122,617	3.49	10.74	0.11	166	6.2	10.4	8.84	140	39	102	50	29	20	108	20	347	154	0.23
Nov 16, 2013	113,611	3.19	8.74	0.18	211	6.9	11.9	10.46	173	49	123	62	45	24	106	20	422	170	0.23
Min	82,451	2.86	8.54	0.11	81	5.9	6.0	7.56	122	34	60	23	19	19	84	18	309	145	0.18
Max	274,383	5.23	15.40	0.41	287	14.6	16.0	15.00	237	67	151	76	59	30	129	23	577	209	0.36
Average	180,655	4.19	12.18	0.20	151	8.3	11.4	9.03	165	46	93	44	32	24	105	20	408	176	0.25
s.d.	64,156	0.70	2.03	0.07	60	2.0	2.4	1.64	33.6	9	28	16	13	3	14	1	80	17	0.05
c.v. (%)	35.5	16.8	16.6	36.3	40.0	24.1	21.1	18.2	20.4	20.7	29.8	36.5	40.2	12.7	13.7	6.8	19.6	9.6	19.0

Note: Minimum (blue), maximum (red), average (bold), standard-deviation (s.d.), and coefficient of variation (c.v.) are also presented. Coefficients of variation are highlighted in a grayscale gradient from lowest (white) to highest (gray).

3.3. Dissolved Major and Trace Ions

3.3.1. Concentrations

Individual and summarized Amazon River anion and cation molar concentrations for all 26 sampling dates are presented in Table 3. All ion concentrations exhibited clockwise hysteresis with respect to discharge except sodium (Na^+), chloride (Cl^-), and rubidium (Rb^+). Na^+ and Cl^- concentrations decreased with increasing discharge and exhibited typical dilution curves with negative b -values (-0.71 and -0.86 , respectively) while Rb^+ exhibited a unique mixed, U-shaped response to discharge (Figure 7). Ion concentrations generally increased to their highest values over the course of the low flow period, or at the early stages of the rising limb (Figure 7). For all ions that exhibited clockwise hysteresis, concentrations were higher during the rising limb (Figure 7, red points) compared to equivalent discharge during the falling limb (Figure 7, blue points). For all major and trace ions, b exponent values were either insignificantly different from 0 or negative (Figure 7).

3.4. LOADEST Fluxes

Annual and mean Amazon River anion and cation fluxes are presented in Table 4. Within the three-year study period, 2011 exhibited the lowest fluxes for all ions (Table 4), primarily due to the lower total discharge that year (Table 2). Despite the relatively low values in 2011, ion fluxes were remarkably stable from year to year (c.v. $< 5\%$), except for uranium (U) which exhibited a coefficient of variation of 8.2% for the study period (Table 4). As a result of the higher relative concentrations during the rising limb of the flood wave (observed as the clockwise hysteresis in Figure 7), nearly all ion fluxes reached their seasonal maximum prior to peak discharge (Figure 8). The notable exceptions were Na^+ , Cl^- , and Rb^+ , which either lacked or displayed unique concentration-discharge hysteresis and consequently exhibited seasonal fluxes that were mostly synchronized with discharge (Figure 8). Of the ions that exhibited clockwise hysteresis, the average phase offsets (days between peak fluxes and peak discharge) for the three study years ranged from 12 to 83 days, with an average of 39 days (Figure 8). Of the ions whose peak fluxes preceded peak discharge, SO_4^{2-} arrived the earliest (83 days) while Ba^{2+} arrived the closest to peak discharge (12 days prior; Figure 8).

3.5. Chromophoric Dissolved Organic Matter Relationships and Fluxes

Chromophoric dissolved organic matter (CDOM) absorption coefficient at 350 nm (a_{350}) ranged from 8.54 to 15.40 m^{-1} , with a mean of 12.18 m^{-1} (Table 3). CDOM absorption coefficients at 254, 350, and 440 nm were strongly positively correlated with DOC concentrations (Figure 9a). The strength of the correlation varied inversely with wavelength, such that the shortest wavelength (a_{254}) exhibited the highest correlation coefficient ($r^2 = 0.91$; Figure 9a). Similar to DOC concentration, a_{350} was strongly positively correlated with discharge, with a nearly identical b -value and correlation coefficient ($b = 0.38$, $r^2 = 0.76$; Figure 9b). Mean annual flux of a_{350} was $74.8 \times 10^{12} \text{ m}^2 \text{ yr}^{-1}$ with a relatively low interannual coefficient of variation (4.2%; Table 2). Mean annual yield and discharge-weighted absorption coefficient were 16.0 years^{-1} and 13.14 m^{-1} , respectively (Table 2). As with DOC, a_{350} fluxes were highly synchronized with discharge (Figure 9c).

3.6. Rock Weathering Inputs

Proportional contributions of silicate (cratonic silicates + shale) and carbonate (dolomite + limestone) rock weathering to Amazon River base cation charge fluxes are shown in Figure 10; all fractional contributions are additionally reported in Table S2. Over the entire time series, base cation charge was predominantly sourced from weathering of carbonate ($62.1 \pm 5.9\%$ of total charge, $n = 26$) and silicate rocks ($24.6 \pm 2.8\%$), with only minor contributions by evaporite dissolution ($3.7 \pm 1.9\%$) and precipitation-derived inputs ($8.8 \pm 2.5\%$). Carbonate weathering was dominated by limestone lithologies ($50.0 \pm 3.0\%$ of total charge) whereas silicate weathering was dominated by cratonic rocks ($23.4 \pm 3.0\%$ of total charge), with only minor contributions by Andean shale lithologies ($1.2 \pm 0.4\%$ of total charge).

The estimated annual average CO_2 consumption yields over our study period are $(2.03 \pm 0.09) \times 10^5 \text{ mol CO}_2 \text{ km}^{-2} \text{ yr}^{-1}$ for carbonate rock weathering and $(1.52 \pm 0.02) \times 10^5 \text{ mol CO}_2 \text{ km}^{-2} \text{ yr}^{-1}$ for silicate rock weathering ($n = 26$). When combined, the average total weathering CO_2 consumption yield estimate was $(3.55 \pm 0.11) \times 10^5 \text{ mol CO}_2 \text{ km}^{-2} \text{ yr}^{-1}$.

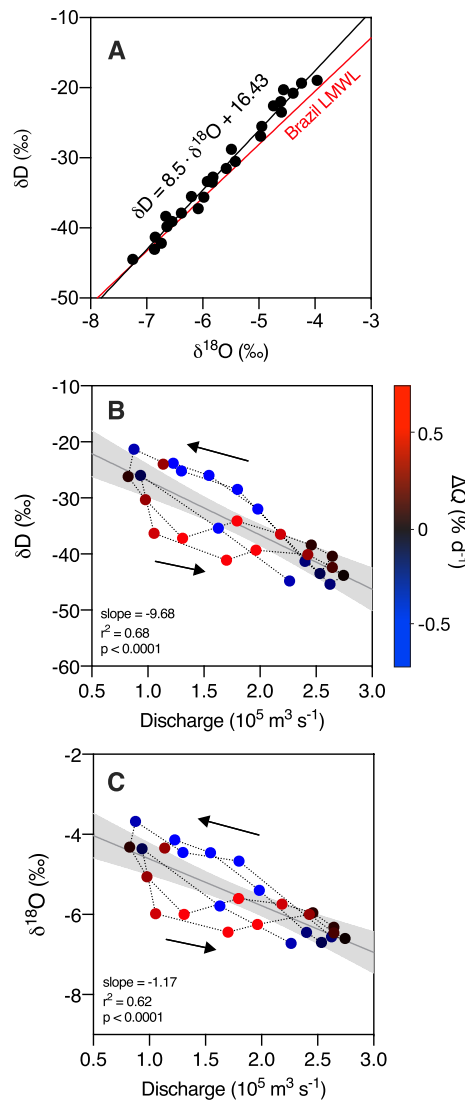


Figure 4. (a) Stable isotopes ratios of water (δD , $\delta^{18}O$) in Amazon River samples collected from 2011 to 2013. Brazil Local Meteoric Water Line ($\delta D = 8.6 \cdot \delta^{18}O + 9.9$; IAEA/WMO, 2020) shown in red with linear regression of Amazon samples shown in black. Panels (b) and (c) show δD and $\delta^{18}O$ versus instantaneous discharge, respectively, with linear regressions (gray line) and 95% confidence intervals (light gray bands). δD and $\delta^{18}O$ data points are colored by instantaneous change in discharge with red indicating an increasing flow (rising limb) and blue indicating decreasing flow (falling limb).

was higher than previous values from Óbidos and the mouth of the river (+8.9–11.2‰; Salati et al., 1979; Longinelli & Edmond, 1983) and indicates the effect of significant evaporative recycling within the basin compared to precipitation d -excess (+9.8) (Martinelli et al., 1996, Gat & Matsui, 1991). The high d value from evaporative recycling also corresponds well with the prevalence of discharge:precipitation ratios < 1.0 (Figure 2b). Given the high temporal resolution sampling used in this study, we were able to detect the strong seasonal depletion of deuterium and ^{18}O with the annual flood pulse (Figures 4b and 4c). This seasonal depletion corresponds to both higher relative inputs from precipitation compared to baseflow during peak discharge (Mortatti et al., 1997) and to the lower isotopic signature of precipitation during the wet season from mid-December to mid-May, which generates the runoff that comprises the flood pulse (IAEA/

4. Discussion

4.1. Amazon River Discharge Dynamics

Mean annual Amazon River discharge at Óbidos for the three study years ($180,940 \text{ m}^3 \text{ s}^{-1}$) was slightly higher but comparable to the interannual average since 1902 ($163,000 \text{ m}^3 \text{ s}^{-1}$; Caldele et al., 2002). Discharge varied inversely with the Oceanic Niño Index (Figure S3), a measure of the El Niño-Southern Oscillation phenomenon (calculated as the running three-month average monthly sea temperature anomaly for the east-central tropical Pacific), which is coupled to the 2–3 years precipitation and discharge cycles observed in the Amazon Basin (Richey, Nobre, et al., 1989). The increase in total annual discharge after 2011 is thus likely a result of the moderate to strong La Nina ($ONI < -1.0^\circ$), the effects of which would have started at Óbidos in late 2011 and extended into mid 2012 (Figure S2).

The consistently strong counter-clockwise precipitation-discharge hysteresis observed for the years 2009–2016 indicates a significant residence time for water that falls as precipitation within the basin prior to riverine export (Figure 2b). Previous modeling studies have inferred that similar hysteresis is caused by storage of water within a slow-flow reservoir, such as groundwater (Andermann et al., 2012). In the case of the Amazon, basin-scale hydrologic modeling has shown that the majority (56%) of terrestrial water storage is controlled by surface water, while soil and groundwater comprise the remaining 36% and 8%, respectively (de Paiva et al. 2013). These results highlight the role of surface waters and in particular the extensive floodplains along the mainstem in regulating the amplitude and timing of the annual flood wave (Junk, 1997; Richey, Mertes, et al., 1989). The discharge versus precipitation results from this study also show that annual precipitation is approximately double annual discharge, suggesting that half of the rain that falls within the basin upstream of Óbidos is lost via evapotranspiration. This discharge:precipitation ratio is identical to previous estimates that found that 50% of Amazonian precipitation is recycled (Salati & Vose, 1984).

Discharge-weighted annual mean δD and $\delta^{18}O$ values observed in this study (-35.8 and -6.1‰ , respectively) correspond well with previous mean values recorded near the mouth of the river (-34.6 and -5.6‰ , respectively; Salati et al., 1979). Our observed range of $\delta^{18}O$ values (-4.0 to -7.3‰ ; Table 1) aligns well with the range previously measured at Óbidos at various discharges (-3.8 to -6.4‰ ; Richey, Mertes, et al., 1989). Minimum δD and $\delta^{18}O$ values observed during peak flows of this study (-44.5 and -7.3‰ , respectively; Table 1) also fall within the range of values observed in mainstem river water near Óbidos during high flows from May to July of previous expeditions (δD : -48.0 to -42.9‰ , $\delta^{18}O$: -7.4 to -6.5 ; Longinelli & Edmond, 1983). Deuterium excess (d), determined via the linear regression of all samples (+16.4‰; Figure 4a),

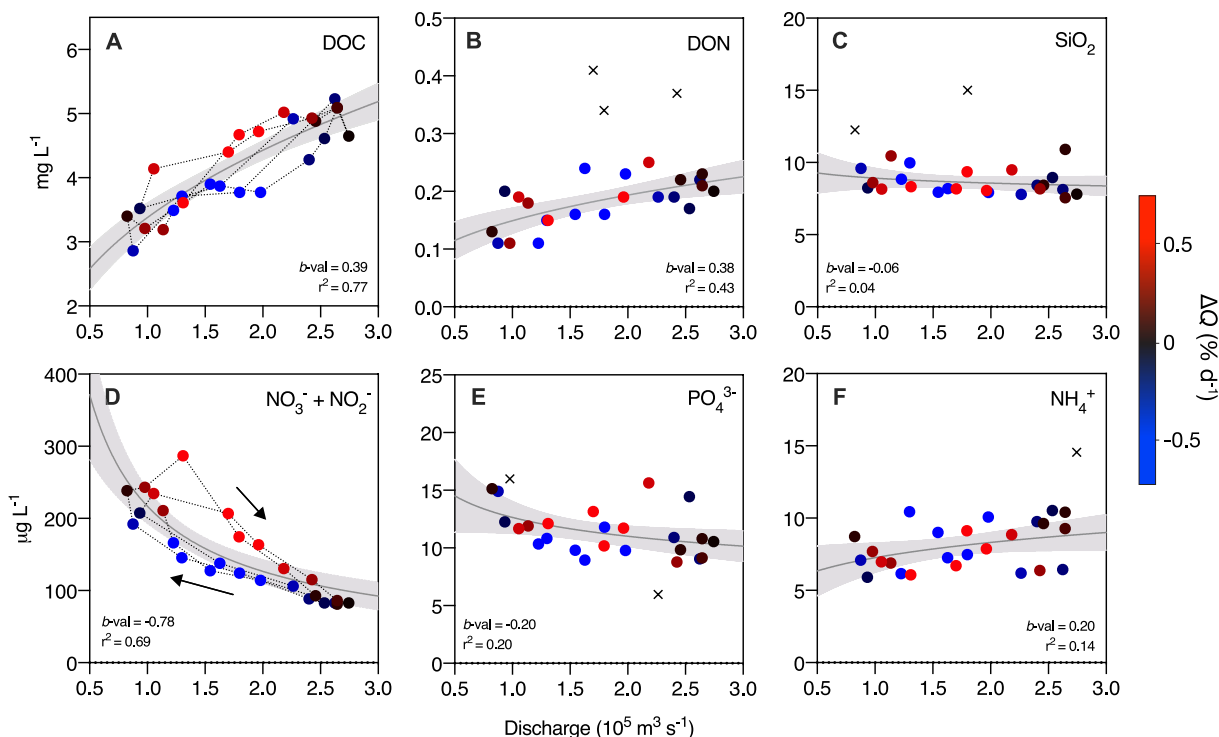


Figure 5. Dissolved organic carbon (a), dissolved organic nitrogen (b), silica (c), nitrate + nitrite (d), orthophosphate (e), and ammonium (f) concentrations versus instantaneous discharge. Linear or power regressions (gray lines) and 95% confidence intervals (light gray bands) are shown. Data points are colored by instantaneous change in discharge with red indicating an increasing flow (rising limb) and blue indicating decreasing flow (falling limb). All concentration units are in mg or μg C, N, or P per liter, except SiO_2 . Statistical outliers are displayed as an “x” and were not included in regression analyses.

WMO, 2020). The slight counter-clockwise hysteresis observed for both δD and $\delta^{18}\text{O}$ indicates that the rising limb consists of proportionately more event water from wet-season precipitation relative to the falling limb and/or that the isotopic signature of rainwater contributing to the flood pulse becomes more enriched over the course of the wet season. Indeed, both mechanisms could contribute to the observed hysteresis as previous studies have shown that $\delta^{18}\text{O}$ of rain becomes significantly more enriched over the course of the wet season (Mortatti et al., 1997; Tardy et al., 2005) and that lagged contributions from baseflow make up a slightly larger proportion of total discharge during the falling limb (Mortatti et al., 1997).

4.2. Refining Dissolved Carbon and Nutrient Concentrations and Fluxes

The range of DOC concentrations observed at Óbidos from 2011 to 2013 ($2.86\text{--}5.23 \text{ mg L}^{-1}$; Table 3) is generally narrower than the range of those measured in the mid-1990s ($2.39\text{--}13.5 \text{ mg L}^{-1}$), which included two extreme values (Moreira-Turcq et al., 2003). Mean values from this study ($4.19 \pm 0.7 \text{ mg L}^{-1}$; Table 3), however, correspond well with the mean of six samples measured from 2010 to 2012 ($3.9 \pm 0.6 \text{ mg L}^{-1}$; Ward et al., 2015) and the mean from the older GEMS-GLORI database (3.67 mg L^{-1} ; Meybeck & Ragu, 1996). Mean DOC concentrations from February to March ($4.84 \pm 0.16 \text{ mg L}^{-1}$), were also nearly identical to those from the Carbon in the Amazon River Experiment (CAMREX) cruises of 1984 for the corresponding months ($4.82 \pm 0.33 \text{ mg L}^{-1}$; Ertel et al., 1986).

The positive b -value in the fitted relationship between DOC concentration and discharge (0.39) indicates that DOC exhibits a mobilization response in the Amazon Basin (Figure 5a). During the wet season, the relative proportion of water from the low DOC Andes headwaters decreases as precipitation flushes accumulated DOC from flooded forests and organic rich litter layers and surface soils in the lowlands (Hedges et al., 2000; Seidel et al., 2016). DOM composition analysis of the Amazon River during high discharge has shown a shift toward more aromatic compounds with higher masses, indicating higher

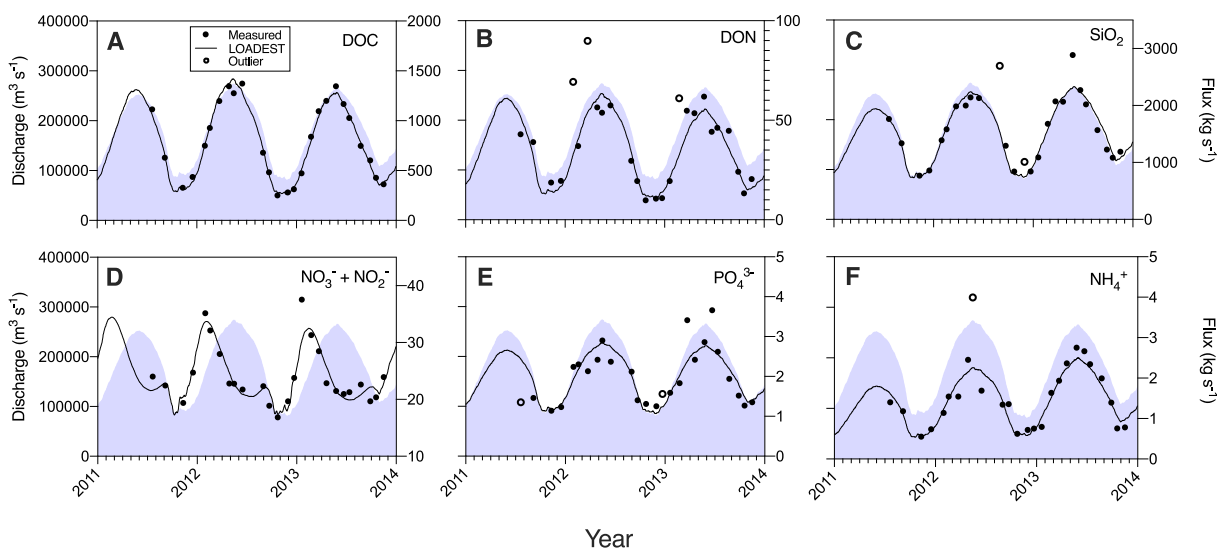


Figure 6. Time series of instantaneous discharge (blue shaded area), LOADEST modeled fluxes (black lines), and measured fluxes (black points) for dissolved organic carbon (a), dissolved organic nitrogen (b), silica (c), nitrate + nitrite (d), orthophosphate (e), and ammonium (f) for years 2011, 2012, and 2013. Open circles denote measured fluxes calculated with statistical outlier concentrations that were not included in the LOADEST model.

inputs from surface runoff and the leaching of material from organic-rich soil horizons and litter layers (Seidel et al., 2016).

Instantaneous DOC fluxes from 2011–2013 ranged from 259 to 1,419 kg s⁻¹ (Figure 6a) and were slightly lower than the range of those calculated in the 1990s (300–2,200 kg s⁻¹), although the two extreme DOC concentration values from the 1990s explain the relatively higher upper limit (Moreira-Turcq et al., 2003). Mean annual DOC flux for this study (25.5 ± 1.0 Tg yr⁻¹) compared well with the estimate from the late 1990s (26.9 Tg yr⁻¹; Moreira-Turcq et al., 2003) and was slightly higher than that reported from the CAMREX cruises (22.1 Tg yr⁻¹; Richey et al., 1990). Global DOC flux to the ocean has been estimated to be 250 Tg yr⁻¹ (Hedges et al., 1997), which would mean the Amazon is responsible for ~10.5% of the global riverine input. Compared to the Congo River Basin, another continent-scale tropical watershed, the Amazon Basin yields 2.15 g more C as DOC per square meter per year (5.45 vs. 3.40 g-C m⁻² yr⁻¹, respectively; Table 2; Spencer et al., 2016). The higher DOC yield from the Amazon is likely a result of the larger proportion of tropical forest (71%) compared to Congo (~50%), which drains expansive savannas and woodland mosaics located in the North and South of the basin (Seyler et al., 2006). Unsurprisingly, the Amazon DOC yield is significantly higher (+3.15 g m⁻² yr⁻¹) than the average of the world's 30 major rivers (2.3 g m⁻² yr⁻¹; Raymond & Spencer, 2015), highlighting the Amazon River as an efficient exporter of terrigenous DOC.

The positive *b*-value in the fitted relationship between DON and discharge (0.38, Figure 5b) suggests that DON, like DOC, exhibits a mobilization response in the Amazon. These results suggest that soluble C- and N-rich organic molecules experience similar mobilization dynamics and may share a common source via the leaching of organic-rich soil horizons and litter layers (Seidel et al., 2016). NO₃⁻ + NO₂⁻ concentrations, on the other hand, exhibited a strong negative correlation with discharge (*b*-value = -0.78, *r*² = 0.69) and a slight clockwise hysteresis, indicating a dilution response and either source-depletion or variable timing of tributary inputs through the annual flood wave (Figure 5d). The hysteresis of NO₃⁻ + NO₂⁻, in which the falling limb exhibited lower concentrations relative to the rising limb, manifested in two annual flux peaks with different amplitudes (first larger then smaller) on the shoulders of the annual flood pulse (Figure 6d). PO₄³⁻ and NH₄⁺ concentrations were seasonally stable, also indicating chemostasis (Figures 5e and 5f, respectively) similar to SiO₂, as discussed below. This chemostatic response indicates that discharge was the dominant control on PO₄³⁻ and NH₄⁺ fluxes, which were consequently synchronized with discharge (Figures 6e and 6f).

Mean DON and DIN (NO₃⁻ + NO₂⁻ + NH₄⁺) concentrations (0.20 mg-N L⁻¹ and 159 μg-N L⁻¹, respectively; Table 3) for this study corresponded closely with reported values from the CAMREX samplings (0.21 mg-N L⁻¹ and 171 μg-N L⁻¹, respectively; Forsberg et al., 1988). Other studies have reported slightly lower

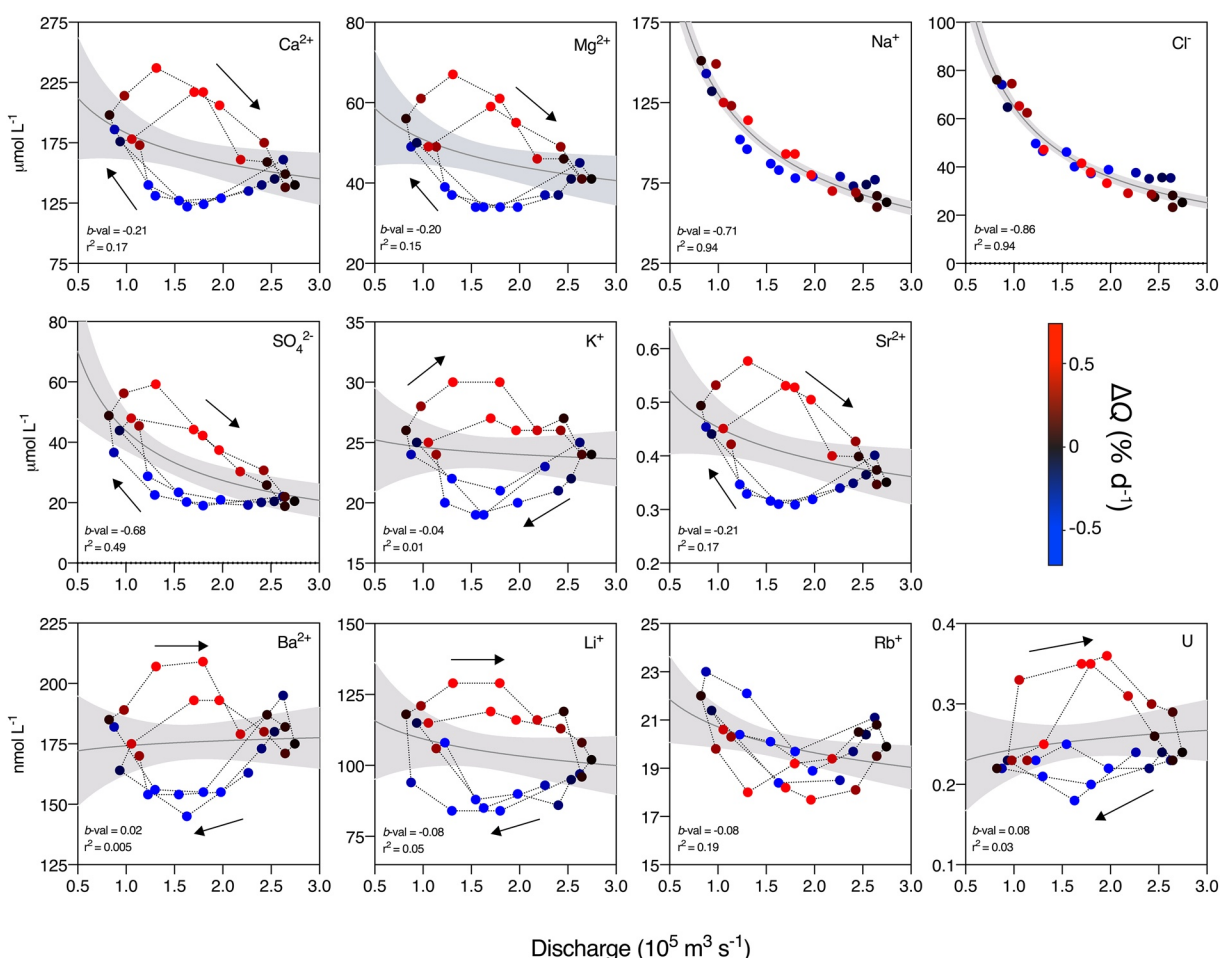


Figure 7. Major and trace ion concentrations versus instantaneous discharge. Data points are colored by instantaneous change in discharge with red indicating an increasing flow (rising limb) and blue indicating decreasing flow (falling limb). Arrows indicate the chronologic progression of ion concentrations which generally exhibit clockwise hysteresis with respect to discharge. Power-law regressions are shown (gray lines) with 95% confidence intervals (light gray bands).

concentrations for NO_3^- (14–126 $\mu\text{g-N L}^{-1}$), although these values are based on small sample sets or single measurements (Dellinger et al., 2015; Meybeck & Ragu, 1996; Stallard, 1980). Published data on PO_4^{3-} are sparse but concentrations reported in this study were slightly lower (5.97–15.98 $\mu\text{g L}^{-1}$, Table 3) than a single reported value at the mouth of the river (21.7 $\mu\text{g L}^{-1}$; Williams, 1968).

Table 4
Annual Major and Trace Ion Fluxes From the Amazon River for Years 2011, 2012, and 2013

	Ca^{2+}	Mg^{2+}	Na^+	Cl^-	SO_4^{2-}	K^+	Sr^{2+}	Ba^{2+}	Rb^+	Li^+	U
	(Tg yr ⁻¹)	(Tg yr ⁻¹)	(Tg yr ⁻¹)	(Tg yr ⁻¹)	(Tg yr ⁻¹)	(Tg yr ⁻¹)	(Gg yr ⁻¹)	(Gg yr ⁻¹)	(Gg yr ⁻¹)	(Gg yr ⁻¹)	(Mg yr ⁻¹)
2011	35.3	6.0	10.9	7.7	15.3	5.4	192	132	9.1	3.9	314
2012	37.6	6.3	11.2	7.8	16.1	5.5	204	142	9.8	4.2	362
2013	37.8	6.4	11.2	7.9	16.2	5.6	205	143	10.1	4.3	364
Average	36.9	6.2	11.1	7.8	15.9	5.5	200	139	9.6	4.1	347
s.d.	1.4	0.2	0.2	0.1	0.5	0.1	7	6	0.5	0.2	28
c.v. (%)	3.8	3.3	1.9	1.2	3.0	2.1	3.6	4.2	5.4	4.8	8.2

Note: Three-year averages are presented in bold with standard-deviations (s.d.) and coefficient of variation (c.v.) below. Coefficients of variation are highlighted in a grayscale gradient from lowest (white) to highest (gray).

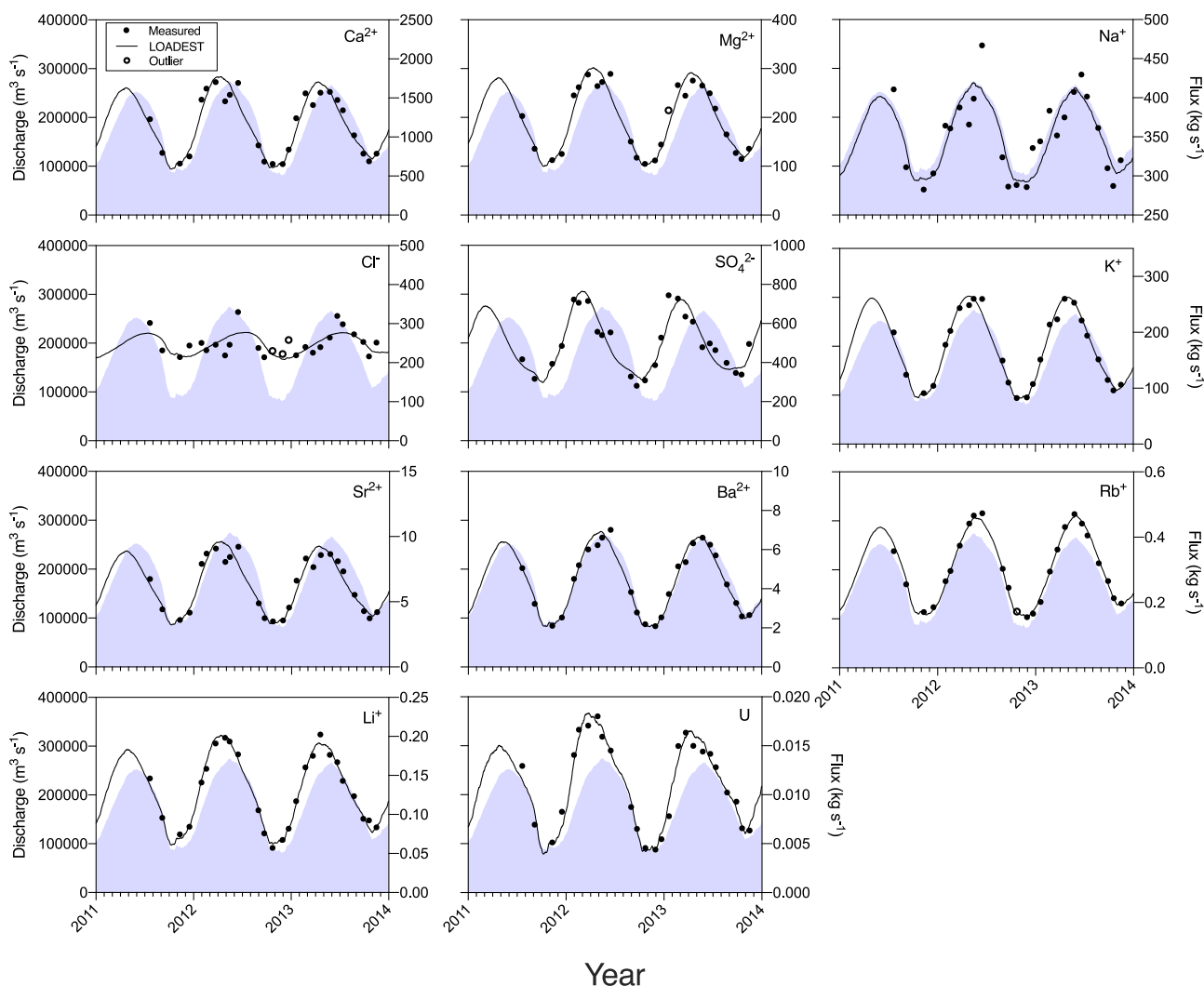


Figure 8. Time series of instantaneous discharge (blue shaded area), LOADEST modeled fluxes (black lines), and measured fluxes (black points) for major and trace ions for years 2011, 2012, and 2013. Open circles denote measured fluxes calculated with statistical outlier concentrations that were not included in the LOADEST model.

Mean DON flux was significantly higher than the value reported from the CAMREX cruise data (1.14 vs. 0.74 Tg-N yr⁻¹, respectively; Table 2), while the mean NO₃⁻ + NO₂⁻ flux was nearly identical to the reported NO₃⁻ flux (776 vs. 771 Gg-N yr⁻¹, respectively; Richey & Victoria, 1993). Mean PO₄³⁻ flux from this study (63.5 Gg-P yr⁻¹; Table 2) was significantly lower than that reported by (Richey & Victoria, 1993; 94 Gg yr⁻¹). We suggest that these discrepancies between DOC, DON, and PO₄³⁻ annual flux estimates are a result of the different sampling intervals and the method of flux estimation. The fluxes generated by the CAMREX cruises were based on only eight instantaneous concentration and discharge measurements taken at various points across the hydrograph of three different years (Richey et al., 1990). Furthermore, Amazon discharge varied considerably during the CAMREX cruises, with an anomalously low water year in 1983 (Richey et al., 1990). Nevertheless, we posit that differences in sampling resolution and flux computation methods rather than interannual variability account for the discrepancies in annual estimates given that C, N, and P fluxes observed in this study were all stable from year to year (c.v. = 2.6-4.4%; Table 2), with the exception of NH₄⁺ (c.v. = 18.7%; Table 2).

Mean SiO₂ concentrations and standard deviations from this study (9.03 ± 1.46 mg L⁻¹; Table 3) compared well with previous reported values (9.79 ± 2.94 mg L⁻¹; Moquet et al., 2016). The observed range

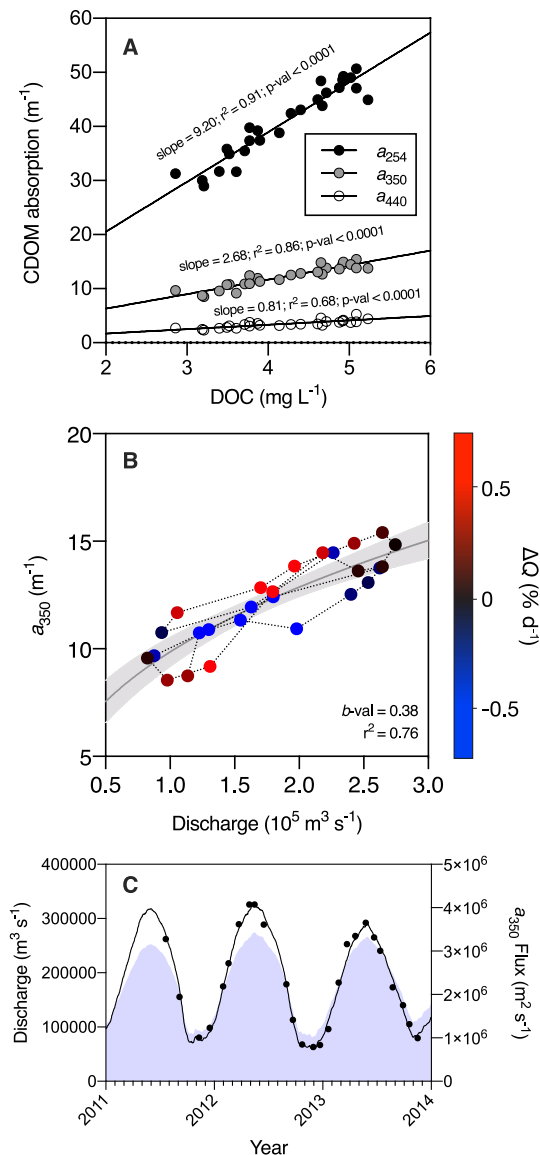


Figure 9. (a) Relationship between dissolved organic carbon concentration and CDOM at three wavelengths (a_{254} , black circles; a_{350} , gray circles; and a_{440} , transparent circles). (b) Relationship between discharge and CDOM absorption at 350 nm (a_{350}). (c) Time series of instantaneous discharge (blue shaded area), LOADEST modeled flux (black line), and measured fluxes (black points) for a_{350} for years 2011–2014.

of SiO₂ concentrations for this study (7.56–15.0 mg L⁻¹; Table 3) also spanned most of the composite range of values from various snapshot studies (6.90–12.20 mg L⁻¹; Dellinger et al., 2015; Meybeck & Ragu, 1996; Stallard, 1980). SiO₂ concentrations did not vary with discharge (b -value = -0.06 ; Figure 5c), indicating chemostasis. Similar SiO₂ chemostatic responses have been observed in small Andean catchments and in larger rivers throughout the basin (Moquet et al., 2016; Torres et al., 2015). Mean instantaneous SiO₂ fluxes and standard deviations ($1,522 \pm 493$ kg s⁻¹; Figure 6c) were slightly lower but generally close to previously reported values ($1,673 \pm 502$ kg s⁻¹; Bouchez et al., 2017). Mean annual flux of SiO₂ from the Amazon at Obidos was 48 Tg yr⁻¹ (Table 2), an estimate that fell between that of Moquet et al. (2016; 58 Tg yr⁻¹), which included fluxes from the Tapajos and Xingu rivers that join the Amazon downstream of Óbidos, and that of Mortatti and Probst (2003) (38.1 Tg yr⁻¹), which is likely low given the low annual discharge during the CAMREX sampling period. Regardless, our estimate equates to $\sim 14\%$ of the global flux of SiO₂ to the ocean (Tréguer et al., 1995). Sub-basin sampling and flux calculations have revealed that the Amazon's central plains (primarily the Solimões-Amazon floodplain) are the main source of Si to the river, either directly via silicate weathering or indirectly via plant decomposition and release (Moquet et al., 2016). Widespread weathering of silicates that are ubiquitously distributed throughout the central plains (in the form of clays or phytoliths) is also consistent with the chemostatic SiO₂ concentration-discharge relationship observed in this study (Moquet et al., 2016).

Overall, the high-resolution sampling, evenly dispersed over the annual hydrographs of two and half years, in concert with the robust LOADEST modeling used in this study has allowed us to compare a time series of contemporary observations with the few available historical measurements from the last four decades. Although this study has significantly updated the historical record of Amazon River C and nutrient fluxes, comparisons with previous data are inadequate to illuminate changes in these fluxes over time. As such, these updated results represent a solid baseline against which to assess the effects of climate change, deforestation, land-use change, and hydroelectric dams into the future.

4.3. Chromophoric Dissolved Organic Matter (CDOM) Export

CDOM represents a major proportion of DOC and plays a fundamental role in aquatic biogeochemistry via photodegradation, impeding sunlight penetration into the water column, and contributing oxidation products (CO and CO₂), as well as being an important tool for the remote sensing of inland waters and as a proxy for terrestrial-derived DOC (Spencer et al., 2008; Del Vecchio & Blough, 2002). The robust CDOM versus DOC

concentration relationships observed in this study suggest that CDOM is a reliable proxy for assessing Amazon DOC concentration and fluxes to the ocean, either remotely via remote sensing platforms or locally via *in situ* CDOM probes (Figure 9a). Similarly robust relationships have been found in other major Arctic, temperate, and tropical rivers (Lambert et al., 2015; Mann et al., 2014; O'Donnell et al., 2012; Stedmon et al., 2011; Yamashita et al., 2010; Spencer et al., 2012, 2013). The Amazon River exhibited a slightly lower a_{350} :DOC slope (2.68; Figure 9a) compared to the Congo River (3.92; Lambert et al., 2015), indicating a lower proportion of CDOM per unit DOC. The slope of the a_{350} :DOC relationship is indicative of DOM aromaticity, which is generally high in tropical rivers as a result of high terrigenous inputs (Lambert et al., 2015; Pérez et al., 2011). Accordingly, our results indicate that the CDOM exported by the Amazon is on average

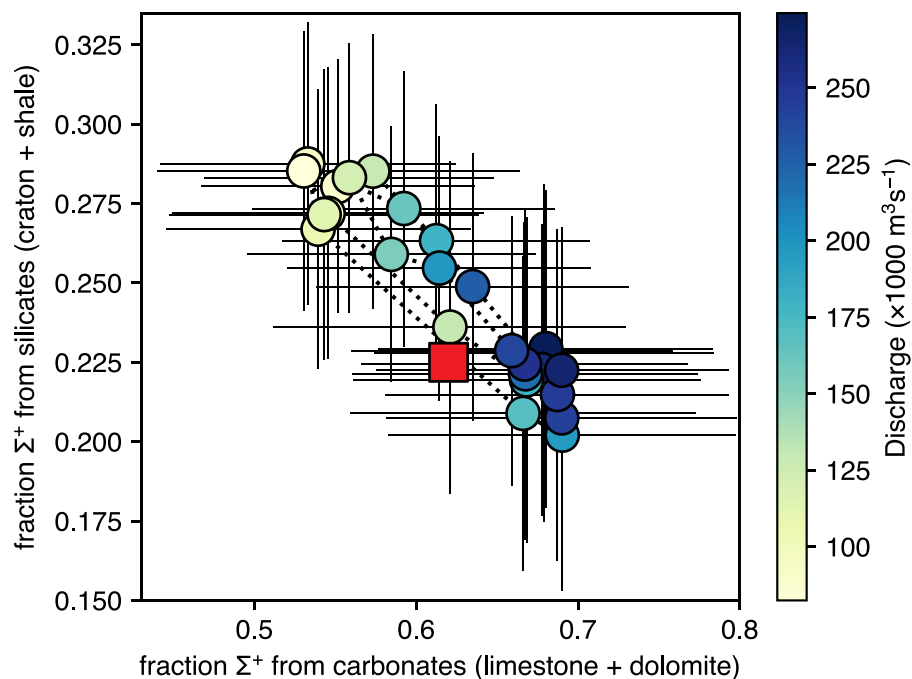


Figure 10. Modeled fraction of base cation charge derived from silicates versus fraction of base cation charge derived from carbonates. Error bars indicate standard deviations of the top 1% of Monte Carlo simulation outputs that exhibited the best fits to data. Data points are colored according to instantaneous discharge from low (yellow) to high (blue) flows. Red point is the value calculated by Gaillardet et al. (1997) for the Amazon River at “high flow” (discharge ranged $258,600\text{--}272,300\text{ m}^3\text{s}^{-1}$ in May 1989, HYBAM).

slightly less aromatic than that of the Congo, which could reflect a difference in either source or processing of DOM within the rivers. This is further supported by the relative proportion of lignin phenols and dissolved black carbon contributing to the DOC pool, which have also been shown to be higher in the Congo River compared to the Amazon River (Spencer et al., 2016; Wagner et al., 2019). Nevertheless, the strong relationship between DOC and CDOM observed in this study shows that CDOM is a consistent fraction of DOC and that by the time DOM transits Óbidos, it is seasonally homogenized and/or broadly uniform in its absorptive properties (i.e. aromaticity).

The mean annual fluxes of a_{350} from the Amazon were found to be more than 20 times that of the Mississippi River (74.8 vs. $3.63 \times 10^{12}\text{ m}^2\text{ yr}^{-1}$) while the yields were nearly 13 times as high (16 vs. 1.25 years^{-1} ; Table 2; Spencer et al., 2013). Amazon a_{350} yields compared closely to the Penobscot and Edisto “blackwater” rivers (18.31 and 12.63 years^{-1} , respectively; Spencer et al., 2013). This sizable flux of CDOM to the western equatorial Atlantic has been detected as a plume with a peak absorption coefficient in July, which lags the Amazon’s hydrograph by approximately one month and constrains the dispersal rate of the river water in the deep tropical North Atlantic to 35 cm s^{-1} (Hu et al., 2004). The establishment of a robust CDOM to DOC relationship in this study should assist in future efforts to examine DOC concentrations in the river and track the C content and dispersal rate of the plume.

4.4. Major and Trace Ion Concentrations, Seasonality, and Export

Overall, major ion concentrations from this study compared well with previously reported concentrations. Mean Ca^{2+} concentration and standard deviation ($164 \pm 34\text{ }\mu\text{M}$; Table 3) were close to those derived from monthly samples taken between 1983 and 2012 for the Hydro-geochemistry of the Amazonian Basin (HYBAM) program ($151 \pm 43\text{ }\mu\text{M}$; Moquet et al., 2016). However, the observed range ($122\text{--}236\text{ }\mu\text{M}$; Table 3) was slightly higher than a composite of smaller datasets ($98\text{--}218\text{ }\mu\text{M}$; Dellinger et al., 2015; Gaillardet et al., 1997; Meybeck & Ragu, 1996; Seyler et al., 2003; Stallard, 1980). Mean Mg^{2+} concentration and standard deviation ($46 \pm 10\text{ }\mu\text{M}$; Table 3) were also highly comparable with previous values from the HYBAM

seasonal sampling ($44 \pm 13 \mu\text{M}$; Moquet et al., 2016) while the range in concentrations ($34\text{--}67 \mu\text{M}$; Table 3) were again slightly higher than a composite range of previous values ($31\text{--}48 \mu\text{M}$; Dellinger et al., 2015; Gaillardet et al., 1997; Meybeck & Ragu, 1996; Seyler et al., 2003; Stallard, 1980). Mean Na^+ concentrations and standard deviations ($93 \pm 28 \mu\text{M}$; Table 3) were also highly comparable to the HYBAM data ($97 \pm 36 \mu\text{M}$; Moquet et al., 2016), while mean Cl^- concentrations and standard deviations ($44 \pm 16 \mu\text{M}$; Table 3) were slightly lower ($58 \pm 26 \mu\text{M}$; Moquet et al., 2016). These patterns held when comparing the ranges of Na^+ and Cl^- ($60\text{--}151$ and $23\text{--}76 \mu\text{M}$, respectively; Table 3) with the composite ranges of previous snapshot studies ($64\text{--}199$ and $31\text{--}210 \mu\text{M}$, respectively; Dellinger et al., 2015; Gaillardet et al., 1997; Meybeck & Ragu, 1996; Seyler et al., 2003; Stallard, 1980). These results suggest that Cl^- concentrations may have been slightly lower than average for the 2011–2013 study period, perhaps as a result of additional dilution from the high discharge during the La Nina period, which increased rainfall and flooding in the Western and Northern Amazon sub-basins. Mean SO_4^{2-} concentration and standard deviation for this study ($32 \pm 13 \mu\text{M}$; Table 3) were nearly identical to the HYBAM values ($32 \pm 15 \mu\text{M}$; Moquet et al., 2016), and the observed range ($19\text{--}59 \mu\text{M}$; Table 3) corresponded well with the composite range from previous studies ($16\text{--}50 \mu\text{M}$; Dellinger et al., 2015; Gaillardet et al., 1997; Meybeck & Ragu, 1996; Seyler et al., 2003; Stallard, 1980). Lastly, mean K^+ concentration and standard deviation ($24.2 \pm 3.1 \mu\text{M}$; Table 3) corresponded closely with those from the HYBAM monitoring ($23 \pm 5 \mu\text{M}$; Moquet et al., 2016). The range of K^+ concentrations ($19\text{--}31 \mu\text{M}$; Table 3) was also very close to the composite range of singular values from previous studies ($20\text{--}28 \mu\text{M}$; Dellinger et al., 2015; Gaillardet et al., 1997; Meybeck & Ragu, 1996; Seyler et al., 2003; Stallard, 1980). Overall, these interstudy comparison results show that average major ions concentrations were stable over the last three decades. However, given the high intra-annual variation in major ion concentrations with the annual flood pulse (c.v. = 12.7–40.2%; Table 3), care must be taken when extrapolating fluxes or weathering rates from small datasets that fail to capture seasonal concentration dynamics.

Trace ion concentrations also generally corresponded well with available previous values. The range of Li^+ concentrations for this study ($84\text{--}129 \text{ nM}$; Table 3) was slightly lower than the range of other mainstem concentrations ($120\text{--}150 \text{ nM}$; Dellinger et al., 2015; Gaillardet et al., 1997). The range of Rb^+ concentrations ($18\text{--}23 \text{ nM}$; Table 3), however, was nearly identical to the range from previous studies ($18\text{--}21 \text{ nM}$; Gaillardet et al., 1997; Seyler et al., 2003). Mean Sr^{2+} concentration and standard deviation ($408 \pm 80 \text{ nM}$; Table 3) corresponded closely with those of a previous study that sampled across multiple seasons and years ($406 \pm 112 \text{ nM}$; Santos et al., 2015). The range of Sr^{2+} concentrations for this study ($309\text{--}577 \text{ nM}$; Table 3) represented the upper end of a composite range from previous studies ($190\text{--}562 \text{ nM}$; Dellinger et al., 2015; Gaillardet et al., 1997; Seyler et al., 2003). The range of observed Ba^{2+} concentrations ($145\text{--}209 \text{ nM}$; Table 3) is nearly identical to a composite range from previous studies ($151\text{--}196 \text{ nM}$; Gaillardet et al., 1997; Seyler et al., 2003). Lastly, the range of observed U concentrations ($0.18\text{--}0.36 \text{ nM}$; Table 3) corresponded well, but was slightly higher than the composite range of previous studies ($0.14\text{--}0.23 \text{ nM}$; Gaillardet et al., 1997; ; Seyler et al., 2003; Palmer & Edmond, 1993). As with the major ions, these trace ion concentration comparison results generally show that the Amazon exhibits low interannual variability. The intra-annual variability of the trace ion concentrations (c.v. = 6.8%–19.6%; Table 3) was somewhat lower than for the major ions, but nevertheless highlights the importance of capturing the range of concentrations across the annual flood pulse.

Major and trace ion concentrations either remained constant or decreased with increasing discharge (zero to negative b -values) indicating either chemostasis or dilution, respectively (Figure 7). Na^+ and Cl^- exhibited the lowest b -values (-0.71 and -0.86 , respectively; Figure 7), consistent with a dominant dilution response and comparable to previous studies in the Amazon Basin (Bouchez et al., 2017; Torres et al., 2015). Ca^{2+} , Mg^{2+} , SO_4^{2-} , and Sr^{2+} exhibited moderately negative b -values ranging from -0.68 to -0.20 , indicating modulated dilution effects, whereas K^+ , Ba^{2+} , Li^+ , Rb^+ , and U all exhibited b -values insignificantly different from zero, indicating chemostasis (Figure 7). Comparable negative to zero b -values have been observed for Ca^{2+} , Mg^{2+} , SO_4^{2-} , and K^+ at Óbidos (Moquet et al., 2016).

All ions except for Na^+ , Cl^- , and Rb^+ exhibited clockwise hysteresis, indicating source depletion and/or variable source-mixing of rapidly mobilized ions transitioning from rising to falling limb (Figure 7). Ion concentration-discharge hysteresis is commonly observed during storm events (House & Warwick, 1998), caused by a time-lag in the supply of dissolved solutes and water from reservoirs or tributaries. Such time-lags can result from variances in dissolution kinetics or transit times within reservoirs (Moquet et al., 2016; House & Warwick, 1998). Sub-basin studies of the Amazon have revealed that total dissolved solid concen-

trations within the three main tributaries (Solimões, Madeira, and Rio Negro) differ from one another but exhibit low annual fluctuations (Moquet et al., 2016). As a result, the downstream ion hysteresis observed in both this study and previously is a product of tributary mixing and temporal offsets in discharge maxima between the main tributaries (Bouchez et al., 2017; Moquet et al., 2016).

Average annual flux of Ca^{2+} and Mg^{2+} (36.9 and 6.2 Tg yr^{-1} , respectively; Table 4) compared closely with both the HYBAM estimates (34 and 6 Tg yr^{-1} , respectively; Moquet et al., 2016) and those from the earlier CAMREX cruises (34.1 and 5.5 Tg yr^{-1} , respectively; Probst et al., 1994). Average annual Na^+ fluxes (11.1 Tg yr^{-1} ; Table 4) also compared closely with the HYBAM and CAMREX estimates (12 and 11.7 Tg yr^{-1} , respectively; Moquet et al., 2016; Probst et al., 1994), however average annual Cl^- fluxes were significantly lower (7.8 vs. 11 and 13.5 Tg yr^{-1} , respectively; Table 4; Moquet et al., 2016; Probst et al., 1994). This discrepancy is likely a result of the relatively low Cl^- concentrations for the 2011–2013 study period and suggests that our flux estimates for Cl^- are conservative. Average annual SO_4^{2-} flux (15.9 Tg yr^{-1} ; Table 4) compared well with the HYBAM flux (16 Tg yr^{-1} ; Moquet et al., 2016) but was significantly lower than that of the CAMREX study (28.5 Tg yr^{-1} ; Probst et al., 1994). The CAMREX flux is likely an overestimate given that it was based on only eight concentrations measured on samples collected over three years that exhibited unusual discharge variation, including an anomalously low water year (1983) during which dissolved ion concentrations were likely high (Richey et al., 1986). Average annual K^+ flux for this study (5.5 Tg yr^{-1} ; Table 4) was exactly halfway between the HYBAM (6 Tg yr^{-1} ; Moquet et al., 2016) and CAMREX (5.0 Tg yr^{-1} ; Probst et al., 1994) estimates. Sampling and flux calculations of individual tributaries to the Amazon have shown that Na^+ , Cl^- , and SO_4^{2-} are primarily supplied by dissolution of carbonates and evaporites and pyrite oxidation in the Andean (Maranon and Ucayali) and foreland Solimões sub-basins (Moquet et al., 2011, 2016). The majority of Ca^{2+} (~78%) is also sourced from the Andean sub-basins (Moquet et al., 2016). Larger proportions of Mg^{2+} and K^+ (~37% and 61%, respectively) are derived from the central plain and shield tributaries, highlighting the role of silicate weathering throughout the lower basin (Moquet et al., 2016).

4.5. Seasonality of Weathering Sources

The higher proportion of base cation charge derived from the weathering of carbonates ($62.1 \pm 5.9\%$) compared to silicates ($24.6 \pm 2.8\%$) is consistent with previous observations (e.g., Gaillardet et al., 1997; Probst et al., 1994; Meybeck & Ragu, 1996; Mortatti & Probst, 2003). Seasonally, carbonate rock weathering contributions to base cation flux exhibited a maximum of ~70% during high-flow conditions, in close agreement with results from the high water periods sampled for CAMREX (74%; Mortatti & Probst, 2003) and a single sample collected at a location near Óbidos during high-flow conditions in 1989 (red square in Figure 10; Gaillardet et al., 1997). In contrast, silicate weathering contributions reached a maximum of ~30% during low-flow conditions (Figure 10). Interestingly, silicate versus carbonate weathering contributions do not display appreciable hysteresis, despite the strong hysteresis observed for individual cation and anion concentrations (Figure 7); rather, contributions fall along a single mixing line as a function of discharge. Comparing the dissolved ion concentration ratios with seasonal data from the Solimões (Devol et al., 1995), Gaillardet et al., (1997) assumed that seasonal variability was low and did not significantly affect the calculated contributions of silicate versus carbonate weathering. This study, however, demonstrates that the source of weathered cations from carbonates and silicates shifts nearly 20% and 10%, respectively, over the annual hydrograph (Figure 10) and confirms the seasonality in proportion of silicate weathering detected in the CAMREX data (Mortatti & Probst, 2003). These observations highlight the necessity of seasonally resolved cation samples to accurately constrain the weathering budget of the Amazon Basin.

Carbonate dissolution has been shown to influence the dissolved base cation load of the Solimões, Madeira, Urucara, Negro, and Trombetas rivers, highlighting the ubiquity of carbonate minerals throughout the basin (Gaillardet et al., 1997). In particular, the Andean sub-basins were found to exhibit the greatest proportions of Ca^{2+} and Mg^{2+} derived from carbonates, presumably sourced from the fractured carbonates and other sedimentary lithologies spread throughout the Solimões, Maranon, and Ucayali watersheds (Gaillardet et al., 1997). Thus, the higher proportion of base cations derived from carbonate weathering during peak flow (~70%) is likely to result from both higher water throughput throughout the basin and within the Andean sub-basins in particular, given their lithologies and ion fluxes (Devol et al., 1995; Gaillardet

et al., 1997; Moquet et al., 2016). In contrast, the higher proportion of base cations derived from silicates during baseflow (~30%) indicates the stronger influence of water from the shield tributaries of the lower basin (i.e. Negro and Trombetas), where a significant quantity of silicate-derived ions are sourced (Devol et al., 1995; Gaillardet et al., 1997; Moquet et al., 2016). In addition to variable and asynchronous inputs from different tributaries (i.e. the Andean vs. lowland sub-basins), the pulse of carbonate-dominant weathering by-products could also arise from the flushing of latent groundwater with the onset of the wet season, since sub-surface waters may have had more time and exposure to weather carbonate minerals. Regardless, future studies should make similar seasonally resolved measurements on all the major tributaries to provide further insight (Torres et al., 2015).

Our estimated shale contributions ($1.2 \pm 0.4\%$ of total charge) are low in the context of previous estimates for the Solimoes and Madeira rivers based on major and trace element concentrations coupled with Sr isotopes (Dellinger et al., 2015). The discrepancy likely results from our estimates relying solely on major and trace dissolved elements. Indeed, teasing apart contributions from igneous rocks and shales based on major and trace dissolved elements is challenging as these two endmembers lack a strong compositional contrast. Instead, Sr isotopes provide a much larger contrast and thus more accurate partitioning of relative igneous rocks and shale inputs. For example, published Sr isotope data for an 8-year time series at Obidos (mean $^{87}\text{Sr}/^{86}\text{Sr} = 0.71154$; Santos et al., 2015) suggest a larger contribution from Andean shale lithologies than our estimates.

The average total annual weathering CO_2 consumption yield calculated here (3.55 ± 0.11) $\times 10^5$ mol CO_2 $\text{km}^{-2} \text{yr}^{-1}$ is slightly higher than that reported in (Probst et al., 1994) (3.1×10^5 mol CO_2 $\text{km}^{-2} \text{yr}^{-1}$) and (Mortatti & Probst, 2003) (3.31×10^5 mol CO_2 $\text{km}^{-2} \text{yr}^{-1}$), but is ~70% higher than that reported in Gaillardet et al., (1997) (2.09×10^5 mol CO_2 $\text{km}^{-2} \text{yr}^{-1}$). Furthermore, the relative proportion of CO_2 consumed by carbonate rock weathering calculated here (57.4%) is slightly lower than that reported in Gaillardet et al., (1997) (66.8%), presumably due to the fact that Gaillardet et al., (1997) only sampled during high-flow conditions, which we observe to be biased toward carbonate weathering relative to other periods of the hydrograph (Figure 10).

5. Conclusions

These results highlight the importance of capturing seasonality of weathering sources and reinforce the potential for biases to occur when sampling the Amazon River system at isolated timepoints. By avoiding this source of error, this study offers a robust baseline comprised of 3 years of seasonally resolved flux data for global biogeochemical models and against which to monitor future change. At Óbidos, the Amazon River represents the integrated signals of numerous large upstream tributaries that drain and deliver dissolved inputs asynchronously from diverse landscapes of mountains, tropical forests, plains, Várzea, and floodplains. In particular, modeling efforts that make use of the integrated signals at Óbidos should keep in mind that they are not representative of a uniform basin. Subsequent studies may opt to further resolve the disparate components of the pulsing Amazon with concurrent high-resolution sampling at the mouths of these large tributaries, which would provide more specific sub-basin level baseline information against which regional anthropogenic change could be more directly assessed.

Data Availability Statement

All data used for the analyses within this manuscript are available in the following repository: <http://doi.org/10.5281/zenodo.4282579>.

Acknowledgments

This work was supported by a grant from the Harbourton Foundation to R. G. M. Spencer and R. M. Holmes. T. W. Drake was supported by ETH Zurich core funding to J. Six. R. G. M. Spencer was additionally supported by NSF OCE-1333157.

References

- Andermann, C., Longuevergne, L., Bonnet, S., Crave, A., Davy, P., & Gloaguen, R. (2012). Impact of transient groundwater storage on the discharge of Himalayan rivers. *Nature Geoscience*, 5(2), 127–132. <https://doi.org/10.1038/ngeo1356>
- Anderson, E. P., Jenkins, C. N., Heilpern, S., Maldonado-Ocampo, J. A., Carvajal-Vallejos, F. M., Encalada, A. C., et al. (2018). Fragmentation of Andes-to-Amazon connectivity by hydropower dams. *Science Advances*, 4(1), eaao1642. <https://doi.org/10.1126/sciadv.aao1642>
- Aufdenkampe, A. K., Mayorga, E., Raymond, P. A., Melack, J. M., Doney, S. C., Alin, S. R., et al. (2011). Riverine coupling of biogeochemical cycles between land, oceans, and atmosphere. *Frontiers in Ecology and the Environment*, 9(1), 53–60. <https://doi.org/10.1890/100014>
- Bouchez, J., Moquet, J.-S., Espinoza, J. C., Martinez, J.-M., Guyot, J.-L., Lagane, C., et al. (2017). River mixing in the Amazon as a driver of concentration-discharge relationships. *Water Resources Research*, 53(11), 8660–8685. <https://doi.org/10.1002/2017wr020591>

- Brown, K. A., Williams, W. J., Carmack, E. C., Fiske, G., François, R., McLennan, D., & Peucker-Ehrenbrink, B. (2020). Geochemistry of Small Canadian Arctic Rivers with Diverse Geological and Hydrological Settings. *Journal of Geophysical Research: Biogeosciences*, 125, 328. <https://doi.org/10.1029/2019jg005414>
- Callede, J., Guyot, J. L., Ronchail, J., Molinier, M., & De Oliveira, E. (2002). L'Amazone à Óbidos (Brésil): étude statistique des débits et bilan hydrologique. *Hydrological Sciences Journal*, 47(2), 321–333. <https://doi.org/10.1080/02626660209492933>
- Coe, M. T., Costa, M. H., & Soares-Filho, B. S. (2009). The influence of historical and potential future deforestation on the stream flow of the Amazon River—Land surface processes and atmospheric feedbacks. *Journal of Hydrology*, 369(1–2), 165–174. <https://doi.org/10.1016/j.jhydrol.2009.02.043>
- Coplen, T. B., & Wassenaar, L. I. (2015). LIMS for Lasers 2015 for achieving long-term accuracy and precision of $\delta^2\text{H}$, $\delta^{17}\text{O}$, and $\delta^{18}\text{O}$ of waters using laser absorption spectrometry. *Rapid Communications in Mass Spectrometry*, 29(22), 2122–2130. <https://doi.org/10.1002/rcm.7372>
- Davidson, E. A., de Araújo, A. C., Artaxo, P., Balch, J. K., Brown, I. F., C. Bustamante, M. M., et al. (2012). The Amazon basin in transition. *Nature*, 481(7381), 321–328. <https://doi.org/10.1038/nature10717>
- Dellinger, M., Gaillardet, J., Bouchez, J., Calmels, D., Louvat, P., Dosseto, A., et al. (2015). Riverine Li isotope fractionation in the Amazon River basin controlled by the weathering regimes. *Geochimica et Cosmochimica Acta*, 164, 71–93. <https://doi.org/10.1016/j.gca.2015.04.042>
- Del Vecchio, R., & Blough, N. V. (2002). Photobleaching of chromophoric dissolved organic matter in natural waters: kinetics and modeling. *Marine Chemistry*, 78(4), 231–253. [https://doi.org/10.1016/s0304-4203\(02\)00036-1](https://doi.org/10.1016/s0304-4203(02)00036-1)
- de Paiva, R. C. D., Buarque, D. C., Collischonn, W., Bonnet, M.-P., Frappart, F., Calmant, S., & Bulhões Mendes, C. A. (2013). Large-scale hydrologic and hydrodynamic modeling of the Amazon River basin. *Water Resources Research*, 49(3), 1226–1243. <https://doi.org/10.1002/wrcr.20067>
- Devol, A. H., Forsberg, B. R., Richey, J. E., & Pimentel, T. P. (1995). Seasonal variation in chemical distributions in the Amazon (Solimões) River: A multiyear time series. *Global Biogeochemical Cycles*, 9(3), 307–328. <https://doi.org/10.1029/95gb01145>
- Dornblaser, M. M., & Striegl, R. G. (2009). Suspended sediment and carbonate transport in the Yukon River Basin, Alaska: Fluxes and potential future responses to climate change: Sediment transport. *Water Resources Research*, 45(6), 382. <https://doi.org/10.1029/2008wr007546>
- Ertel, J. R., Hedges, J. I., Devol, A. H., Richey, J. E., & Ribeiro, M. d. N. G. (1986). Dissolved humic substances of the Amazon River system I. *Limnology & Oceanography*, 31(4), 739–754. <https://doi.org/10.4319/lo.1986.31.4.0739>
- Farella, N., Lucotte, M., Louchouart, P., & Roulet, M. (2001). Deforestation modifying terrestrial organic transport in the Rio Tapajós, Brazilian Amazon. *Organic Geochemistry*, 32(12), 1443–1458. [https://doi.org/10.1016/s0146-6380\(01\)00103-6](https://doi.org/10.1016/s0146-6380(01)00103-6)
- Forsberg, B. R., Devol, A. H., Richey, J. E., Martinelli, L. A., & Dos Santos, H. (1988). Factors controlling nutrient concentrations in Amazon floodplain lakes I. *Limnology & Oceanography*, 33(1), 41–56. <https://doi.org/10.4319/lo.1988.33.1.0041>
- Gaillardet, J., Dupre, B., Allegre, C. J., & Négrel, P. (1997). Chemical and physical denudation in the Amazon River Basin. *Chemical Geology*, 142(3), 141–173. [https://doi.org/10.1016/s0009-2541\(97\)00074-0](https://doi.org/10.1016/s0009-2541(97)00074-0)
- Gaillardet, J., Dupré, B., Louvat, P., & Allègre, C. J. (1999). Global silicate weathering and CO₂ consumption rates deduced from the chemistry of large rivers. *Chemical Geology*, 159(1), 3–30. [https://doi.org/10.1016/s0009-2541\(99\)00031-5](https://doi.org/10.1016/s0009-2541(99)00031-5)
- Gat, J. R., & Matsui, E. (1991). Atmospheric water balance in the Amazon basin: An isotopic evapotranspiration model. *Journal of Geophysical Research*, 96(D7), 13179. <https://doi.org/10.1029/91jd00054>
- Godsey, S. E., Kirchner, J. W., & Clow, D. W. (2009). Concentration-discharge relationships reflect chemostatic characteristics of US catchments. *Hydrological Processes*, 23(13), 1844–1864. <https://doi.org/10.1002/hyp.7315>
- Hastie, A., Lauerwald, R., Ciais, P., & Regnier, P. (2019). Aquatic carbon fluxes dampen the overall variation of net ecosystem productivity in the Amazon basin: An analysis of the interannual variability in the boundless carbon cycle. *Global Change Biology*, 25(6), 2094–2111. <https://doi.org/10.1111/gcb.14620>
- Hedges, J. I., Keil, R. G., & Benner, R. (1997). What happens to terrestrial organic matter in the ocean? *Organic Geochemistry*, 27(5), 195–212. [https://doi.org/10.1016/s0146-6380\(97\)00066-1](https://doi.org/10.1016/s0146-6380(97)00066-1)
- Hedges, J. I., Mayorga, E., Tsamakis, E., McClain, M. E., Aufdenkampe, A., Quay, P., et al. (2000). Organic matter in Bolivian tributaries of the Amazon River: A comparison to the lower mainstream. *Limnology & Oceanography*, 45(7), 1449–1466. <https://doi.org/10.4319/lo.2000.45.7.1449>
- House, W. A., & Warwick, M. S. (1998). Hysteresis of the solute concentration/discharge relationship in rivers during storms. *Water Research*, 32(8), 2279–2290. [https://doi.org/10.1016/s0043-1354\(97\)00473-9](https://doi.org/10.1016/s0043-1354(97)00473-9)
- Hu, C., Montgomery, E., Schmitt, R., & Mullerkarger, F. (2004). The dispersal of the Amazon and Orinoco River water in the tropical Atlantic and Caribbean Sea: Observation from space and S-PALACE floats. *Deep Sea Research Part II: Topical Studies in Oceanography*, 51(10), 1151–1171. [https://doi.org/10.1016/s0967-0645\(04\)00105-5](https://doi.org/10.1016/s0967-0645(04)00105-5)
- Huffman, G. J., Bolvin, D. T., Braithwaite, D., Hsu, K., Joyce, R., Xie, P., & Yoo, S.-H. (2019). NASA global precipitation measurement (GPM) integrated multi-satellite retrievals for GPM (IMERG) [Data set]. docs.server.gesdisc.eosdis.nasa.gov.
- IAEA/WMO. (2020). *Global network of isotopes in precipitation*. [Data set]. Retrieved from <http://www.iaea.org/water>
- Junk, W. J. (1997). General Aspects of Floodplain Ecology with Special Reference to Amazonian Floodplains. In *The Central Amazon Floodplain: Ecology of a Pulsing System*. Ecological Studies, Berlin: Springer.
- Lambert, T., Darchambeau, F., Bouillon, S., Alhou, B., Mbega, J.-D., Teodoru, C. R., et al. (2015). Landscape control on the spatial and temporal variability of chromophoric dissolved organic matter and dissolved organic carbon in large African rivers. *Ecosystems*, 18(7), 1224–1239. <https://doi.org/10.1007/s10021-015-9894-5>
- Longinelli, A., & Edmond, J. M. (1983). Isotope geochemistry of the Amazon Basin: A reconnaissance. *Journal of Geophysical Research*, 88(C6), 3703. <https://doi.org/10.1029/jc088ic06p03703>
- Mann, P. J., Davydova, A., Zimov, N., Spencer, R. G. M., Davydov, S., Bulygina, E., et al. (2012). Controls on the composition and lability of dissolved organic matter in Siberia's Kolyma River basin. *Journal of Geophysical Research*, 117, G01028. <https://doi.org/10.1029/2011jg001798>
- Mann, P. J., Spencer, R. G. M., Dinga, B. J., Poulsen, J. R., Hernes, P. J., Fiske, G., et al. (2014). The biogeochemistry of carbon across a gradient of streams and rivers within the Congo Basin. *Journal of Geophysical Research: Biogeoscience*, 119, 687–702. <https://doi.org/10.1002/2013jg002442>
- Martinelli, L. A., Victoria, R. L., Silveira Lobo Sternberg, L., Ribeiro, A., & Zacharias Moreira, M. (1996). Using stable isotopes to determine sources of evaporated water to the atmosphere in the Amazon basin. *Journal of Hydrology*, 183(3), 191–204. [https://doi.org/10.1016/0022-1694\(95\)02974-5](https://doi.org/10.1016/0022-1694(95)02974-5)

- Meybeck, M. (1982). Carbon, nitrogen, and phosphorus transport by world rivers. *American Journal of Science*, 282(4), 401–450. <https://doi.org/10.2475/ajs.282.4.401>
- Meybeck, M., & Ragu, A. (1996). *River discharges to the oceans: An assessment of suspended solids, major ions and nutrients*, Environment Information and Assessment Report, Paris: UNEP.
- Moquet, J.-S., Crave, A., Viers, J., Seyler, P., Armijos, E., Bourrel, L., et al. (2011). Chemical weathering and atmospheric/soil CO₂ uptake in the Andean and Foreland Amazon basins. *Chemical Geology*, 287(1), 1–26. <https://doi.org/10.1016/j.chemgeo.2011.01.005>
- Moquet, J.-S., Guyot, J.-L., Crave, A., Viers, J., Filizola, N., Martinez, J.-M., et al. (2016). Amazon River dissolved load: temporal dynamics and annual budget from the Andes to the ocean. *Environmental Science & Pollution Research*, 23(12), 11405–11429. <https://doi.org/10.1007/s11356-015-5503-6>
- Moreira-Turcq, P., Seyler, P., Guyot, J. L., & Etcheber, H. (2003). Exportation of organic carbon from the Amazon River and its main tributaries. *Hydrological Processes*, 17(7), 1329–1344. <https://doi.org/10.1002/hyp.1287>
- Mortatti, J., Moraes, J. M., Victoria, R. L., & Martinelli, L. A. (1997). Hydrograph separation of the Amazon river: A methodological study. *Aquatic Geochemistry*, 3, 117–128. <https://doi.org/10.1023/a:1009606801595>
- Mortatti, J., & Probst, J.-L. (2003). Silicate rock weathering and atmospheric/soil CO₂ uptake in the Amazon basin estimated from river water geochemistry: seasonal and spatial variations. *Chemical Geology*, 197(1), 177–196. [https://doi.org/10.1016/s0009-2541\(02\)00349-2](https://doi.org/10.1016/s0009-2541(02)00349-2)
- Musolff, A., Schmidt, C., Selle, B., & Fleckenstein, J. H. (2015). Catchment controls on solute export. *Advances in Water Resources*, 86, 133–146. <https://doi.org/10.1016/j.advwatres.2015.09.026>
- Nobre, C. A., Sampaio, G., Borma, L. S., Castilla-Rubio, J. C., Silva, J. S., & Cardoso, M. (2016). Land-use and climate change risks in the Amazon and the need of a novel sustainable development paradigm. *Proceedings of the National Academy of Sciences*, 113(39), 10759–10768. <https://doi.org/10.1073/pnas.1605516113>
- O'Donnell, J. A., Aiken, G. R., Walvoord, M. A., & Butler, K. D. (2012). Dissolved organic matter composition of winter flow in the Yukon River basin: Implications of permafrost thaw and increased groundwater discharge. *Global Biogeochemical Cycles*, 26, GB0E06.
- Palmer, M. R., & Edmond, J. M. (1993). Uranium in river water. *Geochimica et Cosmochimica Acta*, 57(20), 4947–4955. [https://doi.org/10.1016/0016-7037\(93\)90131-f](https://doi.org/10.1016/0016-7037(93)90131-f)
- Pérez, M. A. P., Moreira-Turcq, P., Gallard, H., Allard, T., & Benedetti, M. F. (2011). Dissolved organic matter dynamic in the Amazon basin: Sorption by mineral surfaces. *Chemical Geology*, 286(3), 158–168.
- Probst, J. L., Mortatti, J., & Tardy, Y. (1994). Carbon river fluxes and weathering CO₂ consumption in the Congo and Amazon river basins. *Applied Geochemistry*, 9(1), 1–13. [https://doi.org/10.1016/0883-2927\(94\)90047-7](https://doi.org/10.1016/0883-2927(94)90047-7)
- Raymond, P. A., & Spencer, R. G. M. (2015). Chapter 11 - Riverine DOM. In D. A. Hansell, & C. A. Carlson (Eds.), *Biogeochemistry of marine dissolved organic matter* (2nd ed., pp. 509–533). Boston: Academic Press.
- Richey, J. E., Hedges, J. I., Devol, A. H., Quay, P. D., Victoria, R., Martinelli, L., & Forsberg, B. R. (1990). Biogeochemistry of carbon in the Amazon River. *Limnology & Oceanography*, 35(2), 352–371. <https://doi.org/10.4319/lo.1990.35.2.0352>
- Richey, J. E., Meade, R. H., Salati, E., Devol, A. H., Nordin, C. F., Jr, & Santos, U. D. (1986). Water Discharge and Suspended Sediment Concentrations in the Amazon River: 1982–1984. *Water Resources Research*, 22(5), 756–764. <https://doi.org/10.1029/wr022i005p00756>
- Richey, J. E., Mertes, L. A. K., Dunne, T., Victoria, R. L., Forsberg, B. R., Tancredi, A. C. N. S., & Oliveira, E. (1989). Sources and routing of the Amazon River Flood Wave. *Global Biogeochemical Cycles*, 3(3), 191–204. <https://doi.org/10.1029/gb003i003p00191>
- Richey, J. E., Nobre, C., & Deser, C. (1989). Amazon river discharge and climate variability: 1903 to 1985. *Science*, 246(4926), 101–103. <https://doi.org/10.1126/science.246.4926.101>
- Richey, J. E., & Victoria, R. L. (1993). C, N, and P export dynamics in the Amazon River. In *Interactions of C, N, P and S biogeochemical cycles and global change* (pp. 123–139). Springer.
- Rose, L. A., Karwan, D. L., & Godsey, S. E. (2018). Concentration–discharge relationships describe solute and sediment mobilization, reaction, and transport at event and longer timescales. *Hydrological Processes*.
- Runkel, R. L., Crawford, C. G., & Cohn, T. A. (2004). Load estimator (LOADEST): A FORTRAN program for estimating constituent loads in streams and rivers. In *US Geological Survey techniques and methods Book 4*. Reston: U.S. Geological Survey.
- Salati, E., Dall'Olio, A., Matsui, E., & Gat, J. R. (1979). Recycling of water in the Amazon Basin: An isotopic study. *Water Resources Research*, 15(5), 1250–1258. <https://doi.org/10.1029/wr015i005p01250>
- Salati, E., & Vose, P. B. (1984). Amazon basin: a system in equilibrium. *Science*, 225(4658), 129–138. <https://doi.org/10.1126/science.225.4658.129>
- Santos, R. V., Sondag, F., Cochonneau, G., Lagane, C., Brunet, P., Hattingh, K., & Chaves, J. G. S. (2015). Source area and seasonal 87Sr/86Sr variations in rivers of the Amazon basin. *Hydrological Processes*, 29(2), 187–197. <https://doi.org/10.1002/hyp.10131>
- Seidel, M., Dittmar, T., Ward, N. D., Krusche, A. V., Richey, J. E., Yager, P. L., & Medeiros, P. M. (2016). Seasonal and spatial variability of dissolved organic matter composition in the lower Amazon River. *Biogeochemistry*, 131(3), 281–302. <https://doi.org/10.1007/s10533-016-0279-4>
- Seyler, P. T., Coynel, A., Moreira-Turcq, P., Etcheber, H., Colas, C., Orange, D., et al. (2006). Organic carbon transported by the equatorial rivers: Example of Congo-Zaire and Amazon basins. In *Soil Erosion and Carbon Dynamics*. (pp. 255–272). Boca Raton: Lewis Publishers, CRC Press.
- Seyler, P. T., Pinelli, M., & Boaventura, G. R. (2003). A first quantitative estimate of trace metal fluxes from Amazon river and its main tributaries. *Journal de Physique IV France*, 107, 1213–1218. <https://doi.org/10.1051/jp4:20030519>
- Spencer, R. G. M., Aiken, G. R., Dornblaser, M. M., Butler, K. D., Holmes, R. M., Fiske, G., et al. (2013). Chromophoric dissolved organic matter export from U.S. rivers. *Geophysical Research Letters*, 40, 1575–1579. <https://doi.org/10.1002/grl.50357>
- Spencer, R. G. M., Aiken, G. R., & Wickland, K. P. (2008). Seasonal and spatial variability in dissolved organic matter quantity and composition from the Yukon River basin, Alaska. *Global Biogeochemical Cycles*, 22(4), 1–13. <https://doi.org/10.1029/2008gb003231>
- Spencer, R. G. M., Butler, K. D., & Aiken, G. R. (2012). Dissolved organic carbon and chromophoric dissolved organic matter properties of rivers in the USA. *Journal of Geophysical Research*, 117, G03001. <https://doi.org/10.1029/2011jg001928>
- Spencer, R. G. M., Hernes, P. J., Dinga, B., Wabakanghanzi, J. N., Drake, T. W., & Six, J. (2016). Origins, seasonality, and fluxes of organic matter in the Congo River. *Global Biogeochemical Cycles*, 30, 1105–1121. <https://doi.org/10.1002/2016gb005427>
- Spencer, R. G. M., Kellerman, A. M., Podgorski, D. C., Macedo, M. N., Jankowski, K., Nunes, D., & Neill, C. (2019). Identifying the Molecular Signatures of Agricultural Expansion in Amazonian Headwater Streams. *Journal of Geophysical Research: Biogeosciences*, 124, 1637–1650. <https://doi.org/10.1029/2018jg004910>
- Spracklen, D. V., & Garcia-Carreras, L. (2015). The impact of Amazonian deforestation on Amazon basin rainfall. *Geophysical Research Letters*, 42, 9546–9552. <https://doi.org/10.1002/2015gl066063>
- Stallard, R. F. (1980). *Major element geochemistry of the Amazon River system*. Doctoral Thesis. Massachusetts Institute of Technology.

- Stedmon, C. A., Amon, R. M. W., Rinehart, A. J., & Walker, S. A. (2011). The supply and characteristics of colored dissolved organic matter (CDOM) in the Arctic Ocean: Pan Arctic trends and differences. *Marine Chemistry*.
- Tardy, Y., Bustillo, V., Roquin, C., Mortatti, J., & Victoria, R. (2005). The Amazon. Bio-geochemistry applied to river basin management. *Applied Geochemistry*, 20(9), 1746–1829. <https://doi.org/10.1016/j.apgeochem.2005.06.001>
- Torres, M. A., West, A. J., & Clark, K. E. (2015). Geomorphic regime modulates hydrologic control of chemical weathering in the Andes-Amazon. *Geochimica et Cosmochimica Acta*, 166, 105–128. <https://doi.org/10.1016/j.gca.2015.06.007>
- Torres, M. A., West, A. J., Clark, K. E., Paris, G., Bouchez, J., Ponton, C., et al. (2016). The acid and alkalinity budgets of weathering in the Andes-Amazon system: Insights into the erosional control of global biogeochemical cycles. *Earth and Planetary Science Letters*, 450, 381–391. <https://doi.org/10.1016/j.epsl.2016.06.012>
- Tréguer, P., Nelson, D. M., Van Bennekom, A. J., Demaster, D. J., Leynaert, A., & Quéguiner, B. (1995). The silica balance in the world ocean: a reestimate. *Science*, 268(5209), 375–379. <https://doi.org/10.1126/science.268.5209.375>
- Tukey, J. W. (1977). *Exploratory data analysis*. Reading: Addison-Wesley.
- Voss, B. M., Peucker-Ehrenbrink, B., Eglinton, T. I., Fiske, G., Wang, Z. A., Hoering, K. A., et al. (2014). Tracing river chemistry in space and time: Dissolved inorganic constituents of the Fraser River, Canada. *Geochimica et Cosmochimica Acta*, 124, 283–308. <https://doi.org/10.1016/j.gca.2013.09.006>
- Wagner, S., Brandes, J., Spencer, R. G. M., Ma, K., Rosengard, S. Z., Moura, J. M. S., & Stubbins, A. (2019). Isotopic composition of oceanic dissolved black carbon reveals non-riverine source. *Nature Communications*, 10(1), 5064. <https://doi.org/10.1038/s41467-019-13111-7>
- Ward, N. D., Krusche, A. V., Sawakuchi, H. O., Brito, D. C., Cunha, A. C., Moura, J. M. S., et al. (2015). The compositional evolution of dissolved and particulate organic matter along the lower Amazon River-Óbidos to the ocean. *Marine Chemistry*, 177, 244–256. <https://doi.org/10.1016/j.marchem.2015.06.013>
- Williams, P. M. (1968). Organic and inorganic constituents of the Amazon River. *Nature*, 218(5145), 937–938. <https://doi.org/10.1038/218937a0>
- Wohl, E. (2020). *Rivers in the landscape* (2nd ed.), Hoboken: John Wiley & Sons.
- Yamashita, Y., Maie, N., Briceño, H., & Jaffé, R. (2010). Optical characterization of dissolved organic matter in tropical rivers of the Guayana Shield, Venezuela. *Journal of Geophysical Research*, 115, G00F10. <https://doi.org/10.1029/2009jg000987>